Forschungszentrum Karlsruhe
in der Helmholtz-Gemeinschaft

Wissenschaftliche Berichte
FZKA 7218

Modeling of Electron-Electron Collisions for Particle-In-Cell Simulations

D. D'Andrea, C.-D. Munz, R. Schneider

Institut für Hochleistungsimpuls- und Mikrowellentechnik
Programm Kernfusion

September 2006

Forschungszentrum Karlsruhe

in der Helmholtz-Gemeinschaft

Wissenschaftliche Berichte

FZKA 7218

Modeling of Electron-Electron Collisions for Particle-In-Cell Simulations

D. D'Andrea, C.-D. Munz [*)], R. Schneider

Institut für Hochleistungsimpuls- und Mikrowellentechnik

Programm Kernfusion

[*)] Institut für Aerodynamik und Gasdynamik, Universität Stuttgart

Forschungszentrum Karlsruhe GmbH, Karlsruhe

2006

Forschungszentrum Karlsruhe GmbH
Postfach 3640, 76021 Karlsruhe

Mitglied der Hermann von Helmholtz-Gemeinschaft
Deutscher Forschungszentren (HGF)

ISSN 0947-8620

urn:nbn:de:0005-072181

Abstract

The modeling of the physics of pulsed plasma thrusters requires the numerical solution of the Boltzmann equation for rarefied plasma flows where continuum assumptions fail. To tackle this challenging task, a cooperation between several institutes has been formed with the goal to develop a hybrid code based on Particle-In-Cell and Direct Simulation Monte Carlo techniques. These development activities are bundled in the project "Numerische Simulation und Auslegung eines instationären gepulsten magnetoplasmadynamischen Triebwerks für eine Mondsonde" which is funded by the Landesstiftung Baden-Württemberg within the subject area "Modellierung und Simulation auf Hochleistungscomputern". In the frame of this project, the IHM is in charge to develop suitable physical-mathematical and numerical models to include charged particle collisions into the simulation, which can significantly affect the parameters of such plasma devices.
The intention of the present report is to introduce the Fokker-Planck approach for electron-electron interaction in standard charged particle simulations, where the impact parameter is usually large resulting in a small deflection angle. The theoretical and applicative framework is discussed in detail paying particular attention to the Particle-In-Cell approach in velocity space, a new technique which allows the self-consistent computation of the friction and diffusion coefficients arising from the Fokker-Planck treatment of collisions. These velocity-dependent coefficients themselves are responsible for the change in velocity of the simulation particles, which is determined by the numerical solution of a Langevin-type equation. Simulation results for typical numerical experiments computed with the new developed Fokker-Planck solver are presented, demonstrating the quality, property and reliability of the applied numerical methods.

Modellierung der Elektron-Elektron Streuung für Particle-In-Cell Simulationen

Überblick

Die Modellierung der Physik von gepulsten Plasmatriebwerken erfordert die numerische Lösung der Boltzmanngleichung für den Fall verdünnter Plasmaströmungen im kinetischen Regime. Um diese herausfordernde Aufgabe zu meistern, ist eine Zusammenarbeit zwischen mehreren Instituten mit dem Ziel zustande gekommen, ein hybrides Rechenprogramm zu entwickeln, das auf "Particle-In-Cell" und "Direct Simulation Monte Carlo" Techniken beruht. Diese Entwicklungsaktivitäten werden im Rahmen des Projektes "Numerische Simulation und Auslegung eines instationären gepulsten magnetoplasmadynamischen Triebwerks für eine Mondsonde" ausgeführt, das von der Landesstiftung Baden-Württemberg durch das Programm "Modellierung und Simulation auf Hochleistungscomputern" finanziert wird. Im Rahmen dieses Projektes fällt dem IHM die Aufgabe zu, geeignete physikalisch-mathematische und numerische Modelle zur Simulation von Stoßprozessen geladener Teilchen in Plasmen zu entwickeln, welche die Betriebsparameter der Triebwerke signifikant beeinflussen können.

Der vorliegende Berichte wurde mit der Absicht verfasst, den Fokker-Planck Ansatz für die Kleinwinkel-Elektron-Elektron Wechselwirkung vorzustellen und diesen in die standardmäßige Simulation geladener Teilchen einzubinden. Das theoretische und handwerkliche Gerüst wird im folgenden ausführlich diskutiert, wobei besonderes Augenmerk auf die "Particle-In-Cell"-Technik im Geschwindigkeitsraum gelegt wird, die es erlaubt, die bei der Fokker-Planck-Behandlung auftretenden Reibungs- und Diffusionskoeffizienten in selbstkonsistenter Weise zu ermitteln. Diese geschwindigkeitsabhängigen Koeffizienten sind ihrerseits für die Geschwindigkeitsänderung der Simulationsteilchen verantwortlich, die sich durch das numerische Lösen einer stochastischen Differentialgleichnung vom Langevin-Typus berechnen lassen. Simulationsergebnisse für typische Testprobleme, die mit dem neu entwickelten Fokker-Planck Löser erzielt wurden, runden den vorliegenden Bericht ab, und geben Auskunft über die Qualität, Eigenschaft und Verlässlichkeit der verwendeten numerischen Methoden.

Contents

1. Introduction 1
2. Fokker-Planck Model for Charged Particles Interactions 5
2.1. Governing Equations 5
2.2. Computation of the Rosenbluth Potentials 6
2.3. Diffusion Process 10
2.4. FP Equation in Spherical Coordinates 12
3. Numerical Solution of Stochastical Differential Equations 14
3.1. Historical Notes 14
3.2. General Ideas and Basic Relations 14
3.3. Itô Formula 16
3.4. Equivalence between the FP and SDE Approach 17
3.5. Itô-Taylor Expansion 18
3.6. Explicit Strong Itô-Taylor Schemes 20
4. Numerical Framework: PIC in Velocity Space 25
5. Results 34
5.1. Experiment 1: Mesh-free / Grid-based Interface Handling. 34
5.2. Experiment 2: Grid-based Approximations (Rosenbluth Solver) 34
5.3. Experiment 3: Mesh-free Approximations (Langevin Solver) 36
5.4. Experiment 4: Interplay of the different Building Blocks (Fokker-Planck Module) 40
5.5. Arbitrary Isotropic Initial Distribution. 47
6. Outlook 50
References 52
Appendix A. Boltzmann Collision Integral and Fokker-Planck Approximation 54
Appendix B. Differential Rutherford Scattering Cross Section 56
Appendix C. Short-time Solution of the FP equation 57
Appendix D. Three Dimensional Solution of the Lenard-Bernstein Model 59
Appendix E. Some Properties of the Rosenbluth Potentials 61
Appendix F. Fourier Transformation of the Coulomb Potential 62
Appendix G. Approximate Multiple Stratonovich Integrals 63

1. Introduction

The present work is a piece of a much bigger puzzle whose final picture will be the development of a hybrid **P**article-**I**n-**C**ell (PIC) / Direct Simulation Monte Carlo (DSMC) code (working title: PICLAS) for the investigation of the physics of a **P**ulsed **P**lasma **T**hruster (PPT) [2]. For that purpose, a cooperation between IRS (Institute of Space Systems, University of Stuttgart), IAG (Institute for Aerodynamics and Gas Dynamics, University of Stuttgart), HLRS (High Performance Computing Center Stuttgart) and IHM (Institute for Pulsed Power and Microwave Technology, Research Center Karlsruhe) has been formed to tackle this really challenging task.

A PPT is a kind of thruster which uses a different principle to push an object in the space: the classical view of huge tanks burning tons of liquid hydrogen expanding in nozzle, must now be abandoned in favor of a small box connected to two electrodes emitting a nice blue plume when tested in a vacuum chamber. This way to move in space is called electric propulsion. According to a classical definition [22] the electric propulsion is "the acceleration of gases for the purpose of producing propulsive thrust by electric heating, electric body forces, and/or electric and magnetic body forces". For more information about this topic we refer the interested reader to the book of Jahn [22].

In order to understand why the rocketry researchers are interested in such unconventional devices, it might turn useful to review very shortly the basics of aerospace propulsion [40]. The mother of all rocketry equations is no doubt, the Tsiolkowsky equation

$$\Delta v_{\mathrm{mis}} = v_{\mathrm{exh}} \ln\left(\frac{m_{\mathrm{i}}}{m_{\mathrm{f}}}\right) ,$$

where m_{i}, m_{f} and v_{exh} denote the initial and final mass of the propellant and the exhaust velocity, respectively. The Δv_{mis} is the integration over time of the magnitude of the acceleration and deceleration by using only the rocket engine. Although an extreme simplification, the rocket equation captures the essentials of rocket flight physics in a single short equation. The change of the mission velocity Δv_{mis} is the most important quantity in orbital mechanics because it quantifies how difficult in terms of energy it is to go from one trajectory to another; to achieve large Δv_{mis}, consuming a reasonable quantity of fuel, the exhaust velocity must be very large. This brief overview on some rocketry parameters brings to the conclusion that if one wants really to explore the deep space, then propulsion systems which are capable of producing very large v_{exh} must be developed. In other words the limitations intrinsic in the chemical propulsion must be overtaken. In fact we cannot do any better than breaking a chemical bound and converting its energy in kinetic energy in a totally adiabatic way. On the contrary, charged particles can be accelerated in principle up to the speed of light.

Since more than two decades, the IRS has started a "small satellite" program, in whose frame a lunar satellite is under development. Mission BW-1 will be accomplished by a PPT, named SIMPLEX (**S**tuttgart **I**nstationary **M**agneto**p**lasmadynamic Thruster for **L**unar **Ex**ploration). In this frame, a PPT is a natural choice for its properties of compactness, reliability and ease

of construction. Moreover the pulsed energy release allows for low average power without loss of performances, a tight constrain on board small satellites [35]. As illustrated in Figure 1.1 a condensator charges the electrode to a potential difference which , thanks also to a common sparkle ablates a layer of the block of Teflon (PTFE). The charged particles will move because of the electric fields and will self-induce a magnetic field. The Lorentz force that is born by the interaction of the electric and magnetic fields will push the particles outside of the truster. Having this device changed the momentum of the particles it will get an equal and opposite reaction. The ignition process is very complex still not completely understood; candidate pro-

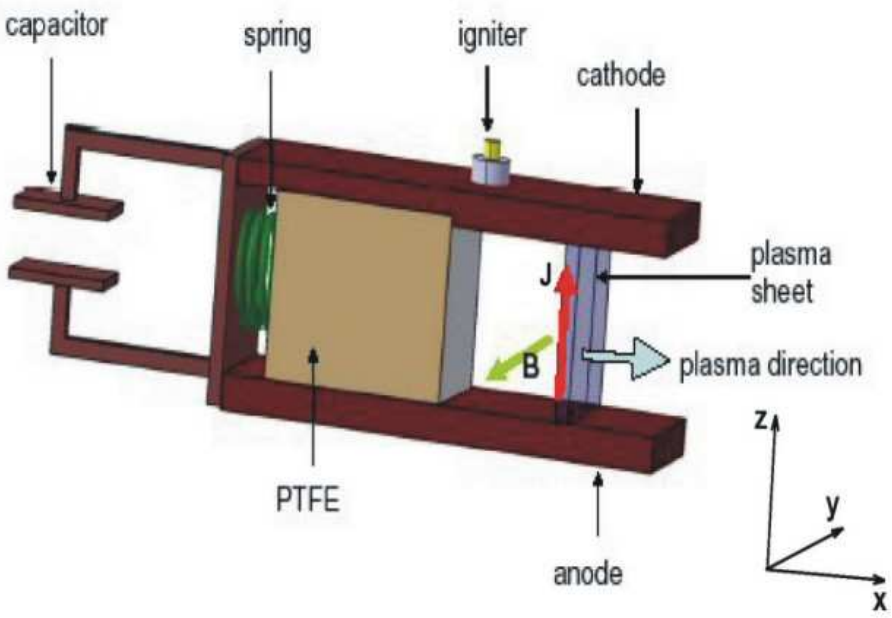

FIGURE 1.1. Schematic representation of a PPT. Technical specifications [34]: Single pulse duration: 8μs; current: 30 kA; exhaust velocity: 12 km/s; specific impulse: 1200 s.

cesses are the initial plasma discharge near the propellant surface and the ultraviolet radiation from the igniter. No matter what, the discharge becomes an arc, with the voltage between the electrodes dropping to hundreds of volts. The rising current creates the sufficient heat transport at the low particle densities to overcome the tendency for current concentration in regions of higher plasma temperature installing an ideally diffused arc. Typically, the PPT plasma consists of electrons and heavy particles (neutrals, positives and negatives) in quasi neutrality condition. Non-equilibrium conditions exist in several degrees and kinds because the downstream vacuum permits high velocities and low densities. Possible local equilibrium can be realized in proximity of the propellant surface where velocities are low and densities high, although the temperatures can vary from specie to specie [8]. In other words, it is not possible to use the moments of the Boltzmann equation and the phase space distribution must approximated mathematically by means of Dirac distribution functions. With this picture in

mind, it is clear that particle methods [19, 4] are recommended for the simulation of such a device, for its capability in catching charged particles movement in magnetic fields in a self consistent manner.

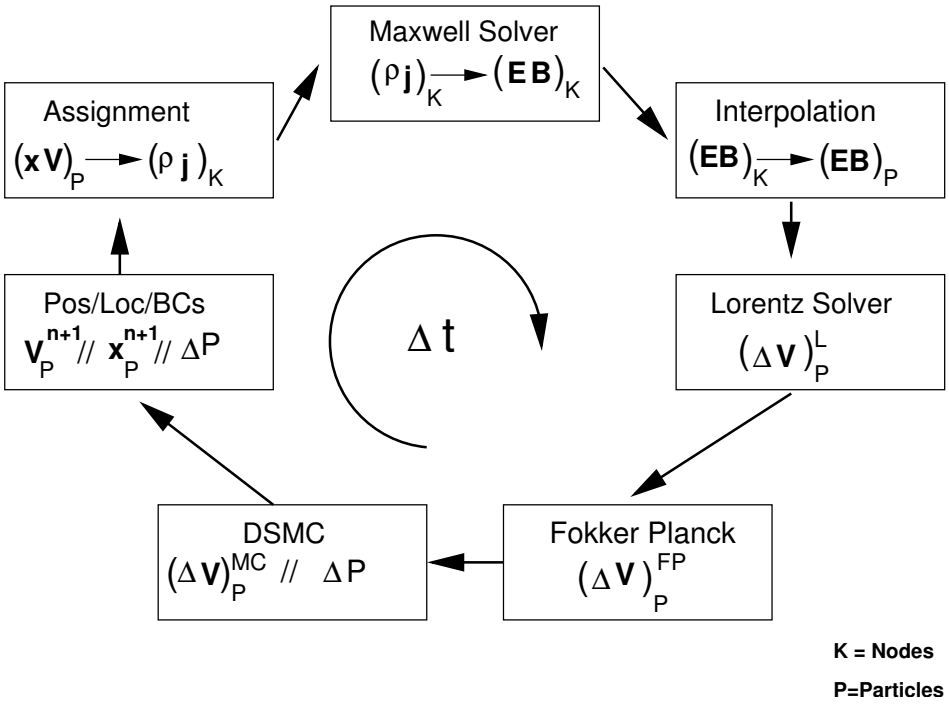

FIGURE 1.2. The different building blocks of the hybrid code PICLAS (Pos/Loc/BCs means Posistion/Localization/Boundary Conditions).

In order to model the physics of the PTT, the PIC code developed by IHM [32, 33] has to be extended by means of models for binary intraspecies charged particle collisions and binary interspecies reactions. A coupling cycle of the integrated hybrid code PICLAS is seen in Figure 1.2, which consists of four main building blocks: (A) Maxwell solver [31], (B) Lorentz solver [32], (C) Fokker-Planck block (see below), and (D) DSMC part [26, 2] for the treatment of chemical reactions. Note, that part (A) represents a finite volume scheme, based on an unstructured computational grid while the blocks (B)-(D) are particle based systems involving the spatial grid only to determine possible particle interactions. Moreover, interpolation and assignment techniques form another main constituent of the coupling [14]. For a given particle distribution within the computational domain, the charge and current densities define the electromagnetic eigenfields. Therefore, their values at the particle positions have to be assigned to node or cell values for the Maxwell solver, where they act as source terms. After completing the Maxwell step, the electrical field and the magnetic induction are known as cell averages in the finite volume context. They have to be evaluated at the particle positions to determine the Lorentz forces acting on the charged particles. Hence, the field values have

to be interpolated from grid positions to particle positions with the desired order of accuracy. The Lorentz solver then determines the acceleration of the particles. Next, Fokker-Planck and DSMC steps determine additional velocity changes of the charged as well as uncharged particles due to elastic and inelastic interactions. These steps, as well as the Lorentz solver, act on the same particle distribution, i.e. the distribution at the beginning of the time step. Each step changes the velocity of the particles without actually moving them. The movement of the particles is done in a separate pushing step which determines the changed distribution function of the different particles species. Within this step, the particles have to be localized with respect to the spatial grid to assign the charge and current densities to the nodes and/or barycenters of the computational mesh. Furthermore, this information is also important for the application of the correct boundary conditions. Finally, this closes the self-consistent determination cycle, which have to be run through at each time step of the simulation.

Coulomb interaction between charged particles like electron-electron collisions play an important role in many application areas of plasma physics and accelerator physics. For the thruster under consideration, for example, they can significantly affect the performancies causing momentum and charge losses, the latter due to recombination. Due to the long-range nature of this force, there is a fundamental difference in treating these collisions compared to short-range reactions in the Boltzmann approach of dilute gases and plasmas, where different kind of hard sphere models are important tools of description [3]. The purpose of the present report is to introduce the Fokker-Planck approach for charged particle interaction in PIC simulation, where the impact parameter is usually large and, consequently, the deflection per collision is small. Especially, this diffusion approximation of the Boltzmann collision integral is customary to describe electron-electron interactions in a plasma, which mainly determine the shape of the electron energy distribution function (EEDF). In the case where the energy input into the plasma goes primarily into the thermal part of the EEDF, the high-energy tail is mainly populated by energy up-scattering caused by these collisions. It is clear from energetic considerations, that the high-energy tail also controls reactions like atomic excitation and ionization – the energy sinks for electrons – and to some extent the plasma chemistry. Furthermore, the electron-electron collisions always drive the EEDF towards a Maxwellian distribution. Due to the important role of the EEDF for the plasma properties it is essential to model electron-electron collisions as realistic as possible.

The report is organized as follows: After the introduction of the governing equations and some properties of the Fokker-Planck model in Section 2, the equivalence of this approch to stochastical differential equations is discussed in Section 3. There, also the numerical approximation of these Langevin-type equations is given and numerical schemes are introduced. In Section 4 the numerical framework and implementation issues are sketched out. Afterwards, in Section 5, numerical results are presented which helps to assess the applied numerical schemes. Finally, a short outlook of the further scientific goals are given in Section 6.

2. Fokker-Planck Model for Charged Particles Interactions

2.1. **Governing Equations.** One basic starting point to investigate plasma phenomena is the Boltzmann equation [29, 13]

$$\frac{\partial f_\alpha}{\partial t} + \mathbf{c}\cdot\nabla_x f_\alpha + \frac{\mathbf{K}}{m_\alpha}\cdot\nabla_c f_\alpha = \left(\frac{\delta f_\alpha}{\delta t}\right)_{col} , \tag{1}$$

which describes the evolution of the distribution function $f_\alpha = f_\alpha(\mathbf{x},\mathbf{c},t)$ of plasma specie "α" in phase space. Here, $\mathbf{K} = \mathbf{K}(\mathbf{x},\mathbf{c})$ represents the electromagnetic force acting on the particles of the ensemble "α" with charge q_α and mass m_α. The term on the right-hand side (rhs) of equation (1) is the Boltzmann collision integral which reflects the rate of change with respect to time of f_α due to collisions.

A well-established mathematical description to model the collision contribution is given by the Fokker-Planck (FP) equation [29, 9, 28, 25, 36]

$$\left(\frac{\delta f_\alpha}{\delta t}\right)_{col} = -\frac{\partial}{\partial c_p}\left[F_p^{(\alpha)}\, f_\alpha\right] + \frac{1}{2}\frac{\partial^2}{\partial c_p \partial c_q}\left[D_{pq}^{(\alpha)}\, f_\alpha\right] . \tag{2}$$

This model represents the lowest order approximation of the Boltzmann collision integral, where the leading terms are a consequence of the cut-off for small scattering angles (see Appendices A and B). By passing we note, that equation (1) with the rhs (2) is known as the Landau equation for the distribution function f_α. In the latter equation the coefficients of the dynamical friction force $F_p^{(\alpha)} = F_p^{(\alpha)}(\mathbf{x},\mathbf{c},t)$ (unit: $[m/s^2]$) and diffusion $D_{pq}^{(\alpha)} = D_{pq}^{(\alpha)}(\mathbf{x},\mathbf{c},t)$ (unit: $[m^2/s^3]$), are defined by

$$F_p^{(\alpha)} = \sum_\beta \Gamma_P^{(\alpha\beta)}\, n_\beta(\mathbf{x},t)\, \frac{\partial \mathcal{H}^{(\beta)}}{\partial c_p} \tag{3}$$

and

$$D_{pq}^{(\alpha)} = \sum_\beta \Gamma_P^{(\alpha\beta)}\, n_\beta(\mathbf{x},t)\, \frac{\partial^2 \mathcal{G}^{(\beta)}}{\partial c_p \partial c_q} , \tag{4}$$

respectively, where the index "β" runs over all "scattering" populations (also called field particles). Here, $n_\beta(\mathbf{x},t)$ represents the local density of the scatterer,

$$\Gamma_P^{(\alpha\beta)} = \frac{q_\alpha^2 q_\beta^2}{4\pi\epsilon_0^2 m_\alpha^2}\ln(\Lambda) \tag{5}$$

is the plasma parameter [13] in SI-units ($[\mathrm{m}^6/\mathrm{s}^4]$) and $\ln(\Lambda)$ denotes the Coulomb logarithm (see Appendix B). Note, that the factor $\overline{\nu}_{\alpha\beta} = n_\beta\, \Gamma_P^{(\alpha\beta)} \,/\, v_{\mathrm{th}}^3$ may be considered as an energy-weighted average of the speed-dependent momentum transfer collision frequency (cf. [28]) between the particles of the species "α" and "β", where the thermal velocity is defined by $v_{\mathrm{th}}^2 = k_B\, T_\beta \,/\, m_\beta$. The key quantities to determine the coefficients (3) and (4) are the

Rosenbluth potentials [28] given by

$$\mathcal{H}^{(\beta)}(\mathbf{x},\mathbf{c},t) = \frac{m_\alpha}{m_{\alpha\beta}} \int\limits_{-\infty}^{\infty} \frac{f_\beta(\mathbf{x},\mathbf{w},t)}{|\mathbf{g}|}\, d^3w \,, \tag{6}$$

$$\mathcal{G}^{(\beta)}(\mathbf{x},\mathbf{c},t) = \int\limits_{-\infty}^{\infty} |\mathbf{g}|\, f_\beta(\mathbf{x},\mathbf{w},t)\, d^3w \,, \tag{7}$$

where $1/m_{\alpha\beta} = 1/m_\alpha + 1/m_\beta$ is the reduced mass of the species "α" and "β" and $\mathbf{g} = \mathbf{c} - \mathbf{w}$ is the difference between the velocity of the scattered-off particles (also called test particles) and the velocity of the particles which serve as scatterer (field particles). It is apparent from the latter two expressions that the Rosenbluth potentials and, consequently, the friction force $\mathbf{F}$ and the diffusion tensor $\mathbb{D}$ depend on the velocity $\mathbf{c}$ of test particles. Hence, the FP model represents a complicated nonlinear problem which, in general has to be solved numerically in an appropriate – namely, self-consistent – manner. Note, that the self-consistent approximation includes the situation where the test particles and scatterers are identical. Consequently, the friction and diffusion are a result of a complex interplay among the particles of the complete ensemble which, in addition, depends on the velocity $\mathbf{c}$. An ideal numerical method to tackle this difficult problem represents the PIC technique [19, 4] which will be discussed below. Analytical solutions of the FP equation are available only for very special cases of the friction force and diffusion tensor. For instance, the short-time solution of the FP equation is obtained if one assumes that the friction and diffusion coefficients do not depend on the velocity (see Appendix C). A further analytical solution is known for the Lenard-Bernstein model (also called Ornstein-Uhlenbeck process) which is established by $\mathbf{F} = \mathbb{A}(\mathbf{x},t)\cdot\mathbf{c}$ ($\mathbb{A}$ is a matrix) and $\mathbb{D} = \mathbb{D}(\mathbf{x},t)$ (see, e.g. [12, 15, 20, 37] and also Appendix D).

2.2. **Computation of the Rosenbluth Potentials.** In this section we review approaches to recast the Rosenbluth potentials into an appropriate form which is advantageous for numerical computations.

2.2.1. *The Fourier Transformation Approach.* It is obvious from the relations (6) and (7) that the Rosenbluth potentials are convolutions of the field particle distribution function and the absolute value of the relative speed. This suggest to apply Fourier transformation techniques to compute the integrals, where no assumptions concerning the distribution function have to be imposed. In the following, we consider intra-species scattering which means, that the test and field particles belong to the same type (for instance, electron-electron collision) and drop for convenience the species indices "α" and "β". Performing a change of variables according to $\mathbf{g} = \mathbf{c} - \mathbf{w}$ with $d^3w = -d^3g$ and applying some standard manipulations [17], we obtain the results

$$\hat{\mathcal{H}}(\mathbf{k}) = 8\,\pi \frac{\hat{f}(\mathbf{k})}{k^2} \tag{8}$$

and

$$\hat{\mathcal{G}}(\mathbf{k}) = -8\,\pi \frac{\hat{f}(\mathbf{k})}{k^4} \,, \tag{9}$$

for the transformed quantities with $k = |\mathbf{k}|$, where the identity $\nabla_c^2 g = 2/g$ (see Appendix E) has been used to obtain the second relation. Clearly, the expressions (8) and (9) reveal once again the convolution character of the Rosenbluth potentials: In $\mathbf{k}$-space this leads to the product of the Fourier transform $\hat{f}(\mathbf{k}) = (2\pi)^{-3/2} \int_{-\infty}^{\infty} d^3c \, \mathrm{e}^{-i\,\mathbf{k}\cdot\mathbf{c}} \, f(\mathbf{c})$ and $1/k^2$, which is the analytically obtained Fourier transformation of the "Coulomb potential" $1/g$ (see Appendix F). Since only the derivatives of the Rosenbluth potentials enter in the determination of the friction and diffusion coefficients, we apply the differentiation property of the Fourier transformation and get directly

$$\frac{\partial \mathcal{H}}{\partial c_p} = 8\,\pi\,i\;\mathcal{F}^{-1}\left\{\frac{k_p}{k^2}\hat{f}(\mathbf{k})\right\} \tag{10}$$

and

$$\frac{\partial^2 \mathcal{G}}{\partial c_p \partial c_q} = 8\,\pi\;\mathcal{F}^{-1}\left\{\frac{k_p\,k_q}{k^4}\hat{f}(\mathbf{k})\right\} \tag{11}$$

for the derivatives of the potentials, where $\mathcal{F}^{-1}$ denotes the inverse Fourier transformation of the arguments in the braces. Moreover, this proceeding considerable reduces "computational noise" often associated with differentiation on the velocity grid. In essence, the main advantage of the Fourier approach is that we obtain a first principle, fully self-consistent determination of the deterministic friction (3) and stochastic diffusion (4) since no specific model assumptions on the field particle distribution are necessary to compute the Rosenbluth potentials.

2.2.2. *Hypothesis: Isotropic Field Particle Distribution.* It is well known that the assumption of an isotropic but non-Maxwellian velocity distribution of the field particles implies an enormous reduction of the three dimensional problem [28, 27, 1]. As above, we consider intra-species scattering of charged particles (for instance, electrons) and suppress the species indices "α" and "β". The assumption of isotropic velocity distribution function f $(= f_\beta)$ of the scatterer means that f depends only on the absolute value $w = |\mathbf{w}|$ of the field particle velocity: $f = f(w)$. In order to compute the integrals (6) and (7), we introduce spherical coordinates in velocity space and replace $|\mathbf{c} - \mathbf{w}|$ by

$$|\mathbf{c} - \mathbf{w}| = \sqrt{c^2 + w^2 - 2cw\cos\Theta}\;.$$

The integration over the azimuthal angle Φ and the polar angle Θ yields the results (cf., [29, 28, 27])

$$\mathcal{H}(\mathbf{x}, c, t) = 8\pi\left\{\frac{1}{c}\int_0^c w^2\, f\, dw + \int_c^\infty w\, f\, dw\right\} \tag{12}$$

and

$$\begin{aligned}\mathcal{G}(\mathbf{x}, c, t) \;&=\; 4\pi\left\{\frac{1}{3c}\int_0^c w^4\, f\, dw + c\int_0^c w^2\, f\, dw\right.\\ &+\; \left.\int_c^\infty w^3\, f\, dw + \frac{c^2}{3}\int_c^\infty w\, f\, dw\right\},\end{aligned} \tag{13}$$

where $f = f(\mathbf{x}, w, t)$. To calculate the derivatives of the isotropic potentials in velocity space

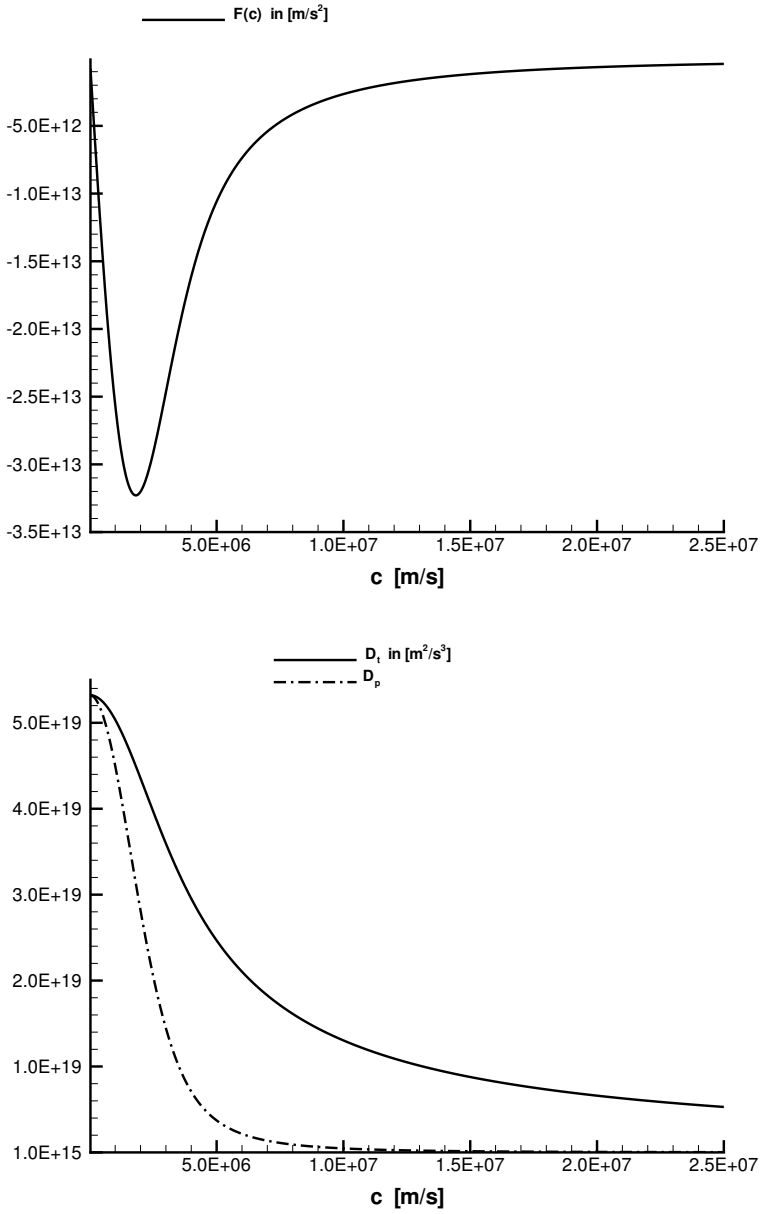

FIGURE 2.1. Dynamical friction (upper plot) and diffusion (lower plot) coefficients $D_\perp$ (full) and $D_\parallel$ (dashed-dotted line) as a function of velocity c.

with respect to the velocity c_p, we use the fact that $\frac{\partial c}{\partial c_p} = \frac{c_p}{c}$ and get the equations

$$\frac{\partial \mathcal{H}(\mathbf{x}, c, t)}{\partial c_p} = \frac{\partial \mathcal{H}(c)}{\partial c}\, \hat{c_p} \tag{14}$$

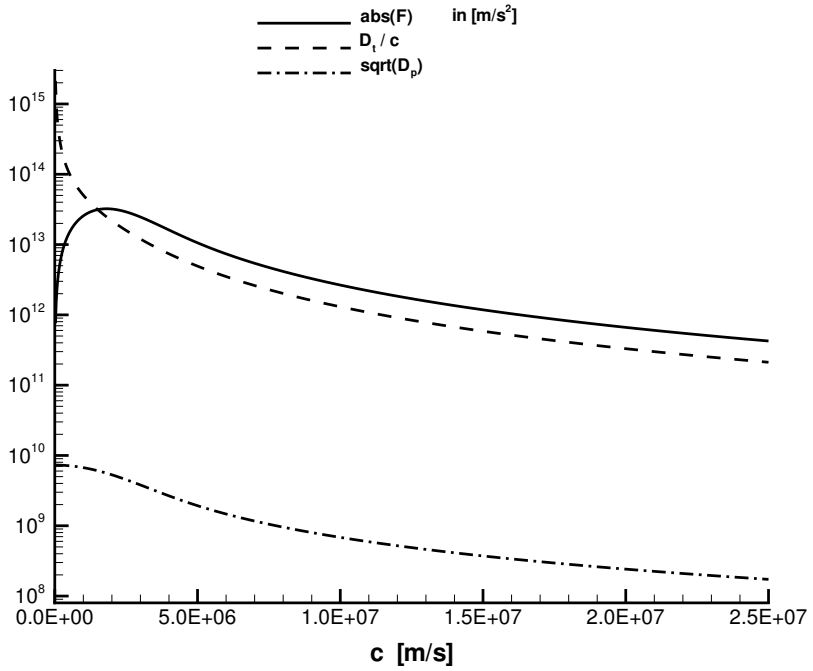

FIGURE 2.2. $|F(c)|$ (full line), $D_\perp(c)/c$ (dashed line) and $\sqrt{D_\parallel}$ (dash-dotted line) as a function of the velocity c. In all cases the unit is $[m/s^2]$.

and

$$\frac{\partial^2 \mathcal{G}(\mathbf{x},c,t)}{\partial c_p \partial c_q} = \frac{\partial^2 \mathcal{G}(c)}{\partial c^2}\,\hat{c_p}\hat{c_q} + \frac{1}{c}\frac{\partial \mathcal{G}(c)}{\partial c}\left[\delta_{pq} - \hat{c_p}\hat{c_q}\right], \tag{15}$$

where δ_{pq} denotes the Kronecker symbol and $\hat{c_p}$ is the p^{th} component of the unit vector $\hat{c} = \mathbf{c}/c$. Then the friction and diffusion coefficients are given by

$$F(c) = n\,\Gamma_P \frac{\partial \mathcal{H}(c)}{\partial c} = -n\Gamma_P \frac{8\pi}{c^2}\int_0^c w^2\, f\, dw\,, \tag{16}$$

$$D_\parallel(c) = n\,\Gamma_P \frac{\partial^2 \mathcal{G}(c)}{\partial c^2} = n\Gamma_P \frac{8\pi}{3}\left\{\frac{1}{c^3}\int_0^c w^4\, f\, dw + \int_c^\infty w\, f\, dw\right\}, \tag{17}$$

$$D_\perp(c) = \frac{n\,\Gamma_P}{c}\frac{\partial \mathcal{G}(c)}{\partial c} = n\Gamma_P \frac{4\pi}{3}\left\{\frac{1}{c^3}\int_0^c (3c^2 - w^2)\, w^2\, f\, dw + 2\int_c^\infty w\, f\, dw\right\}. \tag{18}$$

Clearly, if we identify $\hat{c}$ with the unit vector $\mathbf{e}_x$, then the matrix established by (15) have only non-vanishing diagonal elements. It is obvious, that the coefficients (16)-(18) are decreasing functions of c with high-velocity behavior proportional $1/c^2$, $1/c^3$ and $1/c$, respectively. Consequently, friction and diffusion based effects like approach to equilibrium are much weaker at high energies of the particles. Furthermore note, that field particles with speed w greater than the speed c of the test particles do not contribute to the friction coefficient (16). This effect is a pecularity of Coulomb scattering off an isotropic distribution of scatterers. To

get a quantitative picture, the friction and diffusion coefficients (16)-(18) are seen in Figure 2.1 as a function of the velocity c. For this, a Gaussian distribution function of the form $f(w) = \frac{2}{\sqrt{2\pi}\, v_{\rm th}^3} \exp\!\left(-\frac{w^2}{2v_{\rm th}^2}\right)$ with $v_{\rm th}^2 = k_B\, T/m_e$ is assumed for the field electron distribution, which possesses a constant number density $n_e = 10^{18}$ m^{-3} and a temperature $T_e^\star = 10$ eV. It is apparent from these plots, that the accurate velocity-dependence is very important for modeling these coefficients, especially in the low-velocity region. Furthermore, in Figure 2.2 we depict the dependence of the coefficients $|F(c)|$, $D_\perp(c)/c$ and $\sqrt{D_\parallel(c)}$ (see below) from the velocity c. Note, that these coefficients possess units of an "acceleration" and that $D_\perp(c)/c$ is the dominant contribution at very small velocities, which is responsible that the particles diffuse up towards the thermal velocity $v_{\rm th}$ where they feel strong friction that tends to center the velocity around the mean value.

2.2.3. *Inter-Species Collision: The Electron-Ion Case.* Here, we exploit the fact that the velocity of the electrons is much larger than this one of the ions ($|\mathbf{c}| \gg |\mathbf{w}|$) and, furthermore, the smallness of their mass ratio ($\frac{m_e}{m_{\rm i}} \ll 1$) is taken into account. Clearly, this means, that the electrons are scattered off by infinitely massive ions, where the energy coupling is quite weak. In this situation the Rosenbluth potentials (6) and (7) can be simply approximated by

$$\mathcal{H}^{(\rm i)}(\mathbf{x},\mathbf{c},t) \;=\; \frac{1}{c} \tag{19}$$

$$\mathcal{G}^{(\rm i)}(\mathbf{x},\mathbf{c},t) \;=\; c\,, \tag{20}$$

where it is assumed that $f_{\rm i}(\mathbf{x},\mathbf{w},t)$ is normalized in velocity space. It is straightforward to obtain the components of the friction force and the diffusion tensor, which, respectively, reads as

$$F_p^{(\rm e)}(\mathbf{x},\mathbf{c},t) = \Gamma_P^{(\rm ei)}\, n_{\rm i}(\mathbf{x},t)\, \frac{\hat{c}_p}{c^2} \tag{21}$$

and

$$D_{pq}^{(\rm e)}(\mathbf{x},\mathbf{c},t) = \Gamma_P^{(\rm ei)}\, n_{\rm i}(\mathbf{x},t)\, \frac{1}{c}\left[\delta_{pq} - \hat{c}_p\hat{c}_q\right]\,, \tag{22}$$

where $\hat{c}_p$ is the abbreviation for c_p/c. With the ion charge $q_{\rm i} = Z\,e$, the plasma parameter (5) for electron-ion collision is given by

$$\Gamma_p^{(\rm ei)} = Z^2\,\Gamma_p^{(\rm ee)} = \frac{Z^2 e^4}{4\pi\epsilon_0^2 m_{\rm e}^2}\ln(\Lambda)\,, \tag{23}$$

where the parameter Λ for this process is proportional to

$$\Lambda \sim \lambda_D = \sqrt{\frac{\epsilon_0\, k_{\rm B}\, T_{\rm e}\, T_{\rm i}}{e^2\,(n_{\rm e}\, T_{\rm i} + n_{\rm i}\, Z^2\, T_{\rm e})}}\,, \tag{24}$$

where $k_{\rm B}$ is the Boltzmann constant (see Appendix B).

2.3. **Diffusion Process.** A short introduction to stochastical processes is here needed to show how Coulomb collisions can be easily modelled (at expense of heavy algebra) using a stochastic approach. Physical phenomena influenced by stochastical processes like chemical reactions or non-Newton fluid flows are, in fact, quite frequent in nature (see, for instance

[15, 20]). A weakly correlated stochastical process is called a Markov process if the conditional probability density is given by the condition

$$P_n(x_n, t_n|x_{n-1}, t_{n-1};\ \ldots;\ x_1, t_1) = P_2(x_n, t_n|x_{n-1}, t_{n-1})$$

for $t_1 < t_2 < \cdots < t_n$. This means, that the transition probability to $(x_n,\ t_n)$ depends not on the complete history $(x_{n-1},\ t_{n-1};\ldots;x_1,\ t_1)$ but only on the last state $(x_{n-1},\ t_{n-1})$. Then, $P_2(x_n,\ t_n|\ x_{n-1}\ t_{n-1})\ dx_n$ is the probability that, for instance, a particle travels the distance $x_n - x_{n-1}$ during the time $t_n - t_{n-1}$. A well-know example of a Markov process is the decay of unstable nuclei. A central property of a Markov process is that it is completely defined if the probability density $P_1(x_1,\ t_1)$ and the common probability $P_2(x_2,\ t_2|\ x_1,\ t_1)$ – which is also called conditional or transition probability – is given. A special Markov process is realized by the diffusion. Strictly speaking, one is interested in the *short-time* behavior of the transition probability P_2 which is characterized by a diffusion process. This process is defined by the following requirements [15, 20]

$$\int_\Omega d^3u\,(\mathbf{u}-\mathbf{c})_p\,P_2(\mathbf{u}, t+\tau|\mathbf{c}, t) = F_p(\mathbf{c}, t)\,\tau + \mathcal{O}(\tau^2) \tag{25}$$

$$\int_\Omega d^3u\,(\mathbf{u}-\mathbf{c})_p\,(\mathbf{u}-\mathbf{c})_q\,P_2(\mathbf{u}, t+\tau|\mathbf{c}, t) = D_{pq}(\mathbf{c}, t)\,\tau + \mathcal{O}(\tau^2) \tag{26}$$

$$\int_\Omega d^3u\,(\mathbf{u}-\mathbf{c})_{p_1}\ldots(\mathbf{u}-\mathbf{c})_{p_n}\,P_2(\mathbf{u}, t+\tau|\mathbf{c}, t) = \mathcal{O}(\tau^2)\ \ ;\ n>2\ , \tag{27}$$

where τ is a small time step increment. Obviously, these conditions state that the short-time behavior of the diffusion process up to the first order in τ is completely specified by the first two moments of the transition probability P_2 while higher-order moments can be neglected in this order [1]. Moreover, note that the second moment (26) is linear in τ which indicates that the root of the variance – that is the standard deviation – is proportional to $\sqrt{\tau}$. In essence, the requirements (25)-(27) means that the short-time transition probability for given $\mathbf{c}$ and t is normal (Gaussian) distributed with mean value $F_p(\mathbf{c}, t)\,\tau$ and variance $D_{pq}(\mathbf{c}, t)\,\tau$ which obviously, characterize the underlying stochastical process. In order to find the evolution equation of the diffusion process (25)-(27) we follow Honerkamp [20] and start from the expression

$$\int_\Omega d^3c\quad \psi(\mathbf{c})\,\partial_t P_2(\mathbf{c}, t|\mathbf{x}_1, t_1) =$$

$$\lim_{\tau\to 0}\frac{1}{\tau}\int_\Omega d^3c\quad \psi(\mathbf{c})\Big[P_2(\mathbf{c}, t+\tau|\mathbf{x}_1, t_1) - P_2(\mathbf{c}, t|\mathbf{x}_1, t_1)\Big]\ , \tag{28}$$

where $\psi(\mathbf{c})$ is an arbitrary function with the properties that ψ and its first derivative $\nabla\psi$ vanish at the boundary of the domain Ω. Applying to $P_2(\mathbf{c}, t+\tau|\mathbf{x}_1, t_1)$ the relation (which

[1] Note, that either the requirements (25)-(27) are possible or an infinite number of moments are necessary to characterize the process (Theorem of Pawula [42]).

is known as the Chapman-Kolmogorov equation)

$$P_2(\mathbf{c}, t+\tau|\mathbf{x}_1, t_1) = \int d^3u\, P_2(\mathbf{c}, t+\tau|\mathbf{u}, t_2)\, P_2(\mathbf{u}, t_2|\mathbf{x}_1, t_1)\ , \tag{29}$$

performing a Taylor series expansion of $\psi(\mathbf{c})$ arround $\mathbf{c} = \mathbf{u} + \Delta\mathbf{u}$, assuming that $P_2(\mathbf{c}, t+\tau|\mathbf{u}, t_2)$ is normalized with respect to $\mathbf{c}$ and taking into account the definition of the diffusion process (25)-(27), we get

$$\int\limits_{\Omega} d^3c\, \psi(\mathbf{c}) \Big\{ \partial_t P_2(\mathbf{c}, t|\mathbf{x}_1, t_1) + \frac{\partial}{\partial c_p}\Big[F_p\, P_2\Big] - \frac{1}{2}\frac{\partial^2}{\partial c_p \partial c_q}\Big[D_{pq}\, P_2\Big] \Big\} = 0\ , \tag{30}$$

with $F_p = F_p(\mathbf{c}, t)$ and $D_{pq} = D_{pq}(\mathbf{c}, t)$, where also integrations per parts were carried out. Since $\psi(\mathbf{c})$ is an arbitrary function, we conclude that the expression in the curly braces must be zero, and the evolution equation for the transition probability of the diffusion process is established by a FP equation. Note, that the probability density $P_1(\mathbf{c}, t)$, which can be identified with the particle distribution function $f_\alpha(\mathbf{c}, t)$, fulfill the same FP equation. Obviously, this result makes then a link with the Boltzmann integral approximation (2): The charged particles collisions are modeled as a diffusion process that describes the short-time behavior of the interacting system.

2.4. FP **Equation in Spherical Coordinates.** We start with the FP equation in covariant form given by [43]

$$\partial_t f = -\Big[f\, F^\mu\Big]_{,\,\mu} + \frac{1}{2}\Big[f\, D^{\nu\mu}\Big]_{,\,\nu\,,\,\mu}\ , \tag{31}$$

which is valid for any set of curvilinear coordinates x^1, x^2 and x^3 in the non-relativistic case. Here, the commas indicate covariant derivatives with respect to x^μ, repeated Greek indices imply summation (Einstein's summation convention) and $f = f(x^1, x^2, x^3)$ is the particle distribution function. The covariant derivatives can be written as [21, 43]

$$\sqrt{g}\,\Big[f\, F^\mu\Big]_{,\,\mu} = \frac{\partial}{\partial x^\mu}\Big[\sqrt{g}\, f\, F^\mu\Big] \tag{32}$$

and

$$\sqrt{g}\,\Big[f\, D^{\nu\mu}\Big]_{,\,\nu\,,\,\mu} = \frac{\partial^2}{\partial x^\mu \partial x^\nu}\Big[\sqrt{g}\, f\, D^{\nu\mu}\Big] + \frac{\partial}{\partial x^\mu}\Big[\sqrt{g}\, f\, \Gamma^\mu_{\alpha\beta}\, D^{\alpha\beta}\Big]\ , \tag{33}$$

respectively, where $g = |g_{\mu\nu}|$ is the derterminant of the metric tensor $g_{\mu\nu}$ and $\Gamma^\mu_{\alpha\beta}$ denotes the Christoffel symbol of second kind defined by (see, e.g. [45])

$$\Gamma^\gamma_{\alpha\beta} = \frac{1}{2}\, g^{\gamma\delta}\left(\frac{\partial g_{\alpha\delta}}{\partial x^\beta} + \frac{\partial g_{\beta\delta}}{\partial x^\alpha} - \frac{\partial g_{\alpha\beta}}{\partial x^\delta}\right), \tag{34}$$

which, in general, is not a tensor. Inserting (32) and (33) into equation (31), we get after some rearrangements

$$\partial_t \tilde{f} = -\frac{\partial}{\partial x^\mu}\Big[\tilde{f}\left(F^\mu - \frac{1}{2}\Gamma^\mu_{\alpha\beta}\, D^{\alpha\beta}\right)\Big] + \frac{1}{2}\frac{\partial^2}{\partial x^\mu \partial x^\nu}\Big[\tilde{f}\, D^{\nu\mu}\Big]\ , \tag{35}$$

where $\tilde{f} = \sqrt{g}\, f$. Obviously, in the latter equation the drift term (first term on the rhs) is modified by the geometry term $\frac{1}{2}\Gamma^\mu_{\alpha\beta}\, D^{\alpha\beta}$, which vanishes in the case of Cartesian coordinates. In the following we consider spherical polar coordinates in velocity space, where $x^1 = c$, $x^2 = \theta$ and $x^3 = \varphi$. The metric tensor $g_{\mu\nu}$ ($g = c^4\, \sin^2\theta$), the physical components of the vector F^μ

as well as the tensor $D^{\mu\nu}$ and the Christoffel symbols $\Gamma^{\mu}_{\alpha\beta}$ may be adopted from the literature [45], resulting in a quite lengthy expression for the rhs of (35). The first simplification of this expression is obtained by choosing the velocity difference vector $\mathbf{g}$ to be parallel to the unit basis vector $\mathbf{e}_c$. This leads to the fact that the vector $\mathbf{F}$ possesses only the component F_c and the tensor $\mathbb{D}$ is diagonal. Furthermore, assuming azimuthal symmetry, we obtain the equation

$$\begin{aligned} \partial_t \tilde{f} = & - \frac{\partial}{\partial c}\left\{ \tilde{f}\left[F_c + \frac{1}{2c}(D_{\theta\theta} + D_{\varphi\varphi})\right]\right\} + \frac{1}{2}\frac{\partial^2}{\partial c^2}\left[\tilde{f}\, D_{cc}\right] \\ & - \frac{1}{2c^2}\frac{\partial}{\partial \theta}\left[\tilde{f}\, \cot\theta\, D_{\varphi\varphi}\right] + \frac{1}{2c^2}\frac{\partial^2}{\partial \theta^2}\left[\tilde{f}\, D_{\theta\theta}\right], \end{aligned} \tag{36}$$

where $\tilde{f}$ as well as the coefficients F_c, D_{cc}, $D_{\theta\theta}$ and $D_{\varphi\varphi}$ depend on c and θ. A further reduction of the latter equation is obtained if we assume that the friction and diffusion coefficients depend only on the velocity c, then $F_c = F$, $D_{cc} = D_{\parallel}$ and $D_{\theta\theta} = D_{\varphi\varphi} = D_{\perp}$ are given by the relations (16)-(18). The resulting form of the FP equation then reads as (see also [1])

$$\partial_t h = -\frac{\partial}{\partial c}\left[h\left(F + \frac{D_{\perp}}{c}\right)\right] + \frac{1}{2}\frac{\partial^2}{\partial c^2}\left[h\, D_{\parallel}\right] + \frac{D_{\perp}}{2c^2}\frac{\partial}{\partial a}\left[(1-a^2)\,\frac{\partial h}{\partial a}\right], \tag{37}$$

where $h = c^2\, f(c,\theta)$ and a is given by $a = \cos\theta$. Finally, in the case of an isotropic distribution function, where h is independent of the polar angle θ we get the result

$$\partial_t h = -\frac{\partial}{\partial c}\left[h\left(F + \frac{D_{\perp}}{c}\right)\right] + \frac{1}{2}\frac{\partial^2}{\partial c^2}\left[h\, D_{\parallel}\right], \tag{38}$$

which will be considered below in the context of code assessment.

3. Numerical Solution of Stochastical Differential Equations

3.1. **Historical Notes.** In order to study the problem of Brownian motion, Langevin considered the equation

$$\dot{v}(t) = -\gamma\, v(t) + \mathcal{K}(t) \ ,$$

for a particle moving in a suspension with a friction coefficient γ, where $\mathcal{K}(t)$ is a highly irregular force acting on the particle with mass m. From this equation he deduced Einstein's result for the variance of the displacement of the particle – $\mathsf{Var}\{x(t)\} = \frac{2\,k_{\mathrm{B}}\,T}{m\,\gamma}\,t$ –, where he argued that the average (expectation value) of $< x(t)\,\mathcal{K}(t) >$ vanishes because the irregularity of $\mathcal{K}(t)$ (see, [15] and the references given therein). This may be regarded that $\mathcal{K}(t)$ represents a time-dependent "random force", which is a model for the highly fluctuating influence of a very rapid sub-system whose action cancels out in the limit when a large number of particle trajectories are considered. Historically, the Langevin equation was the first example of a (linear) stochastical differential equation (SDE), which represents the so-called Ornstein-Uhlenbeck process [15, 23]. In the context of SDE the Langevin equation is symbolically written as

$$dV(t) = -\gamma\, V(t)\, dt + \sigma\, dW(t) \ ,$$

with $\sigma^2 = 4\,k_{\mathrm{B}}\ T/m$. Here, the change of the stochastical variable $V = V(t)$ within the time step size dt is considered, where the so-called Wiener increment $dW(t)$ "sublimates" the irregular processes mentioned above. Note, as a consequence of the Wiener increment, that the latter equation requires a new mathematical interpretation – this means, the definition of an extended calculus –, which can be consistently introduced for the corresponding integral equation (see, for instance, [15, 23]).

In the following, we focus our attention to generalized Langevin equations, introduce some basic results for SDEs and discuss methods for the numerical solution of SDEs. Furthermore, we will recognize that the numerical solution of SDEs provides a powerful tool to include small-angle Coulomb collisions between charged plasma species into the framework of PIC techniques.

3.2. **General Ideas and Basic Relations.** In this sub-section we consider the straightforward extension of the Langevin equation in one dimension

$$dV(t) = F(V, W, t)\, dt + B(V, W, t)\, dW(t) \ , \tag{39}$$

where the coefficients are functions of the stochastical variable $V = V(t)$ and time t and, in general, also of the Wiener variable $W = W(t)$. Note, that in the case where B is a constant the random forcing is called additive noise, otherwise, if B (linearly) depends on the stochastic quantity $V(t)$ the forcing is called multiplicative noise. The SDE (39) has to be interpreted mathematically as a stochastic integral equation of the form

$$V(t) = V(t_0) + \int_{t_0}^{t} F\Big(V(s), W(s), s\Big)\, dt + \int_{t_0}^{t} B\Big(V(s), W(s), s\Big)\, dW(s) \ . \tag{40}$$

Here, the second term on the rhs is an ordinary integral (of Riemann or Lebesgue type), while the third term is a stochastical integral, which has to be interpreted consistently. The Wiener increment $dW(t)$ appearing in equation (39) and (40) may be defined as an integral over the rapidly fluctuating random term $\eta(t)$ (see, for instance [15, 20])

$$dW(t) = \int_t^{t+dt} \eta(s)\, ds \ , \tag{41}$$

with the requirements that for $t \neq t'$, $\eta(t)$ and $\eta(t')$ are statistically independent, the mean value$< \eta(t) >= 0$ and and the variance $< \eta(t)\,\eta(t') >= \delta(t - t')$. For our purposes, we introduce the Wiener increment by considering the sequence $\Big\{\eta_i\Big\}_{i\in\mathbb{N}}$ of independently and identically distributed random numbers with the expectation values $\mathbb{E}\{\eta_i\} = 0$ and $\mathbb{E}\{\eta_i^2\} = 1$ [short notation: $\eta_i \sim iid(0,1)$] and define

$$W^N(t_n) = \frac{1}{\sqrt{N}} \sum_{i=1}^{n} \eta_i \ ; \quad t_n = \frac{n}{N} \ \ , 0 \leq n \leq N \tag{42}$$

with $\Delta t_i = t_{i+1} - t_i = 1/N$. Then, the Wiener increment reads as

$$\Delta W_i = W_{i+1} - W_i = \frac{1}{\sqrt{N}}\, \eta_{i+1} = \sqrt{\Delta t_i}\, \eta_{i+1} \ , \tag{43}$$

and possess the properties $\mathbb{E}\{\,\Delta W_i\,\} =< \Delta W_i >= 0$ and $\mathbb{E}\{\,\Delta W_i\ \Delta W_j\,\} =< \Delta W_i\ \Delta W_j >= \Delta t_i\, \delta_{ij}$, where the latter relation indicates that the variance is linear in Δt_i. Now, setting in the integral equation (40) $V(t_0) = F = 0$ and replacing B by the random function $G = G\Big(W(t), t\Big)$, we obtain the formal definition of the Itô integral:

$$\mathrm{I}[G] = \int_{t_0}^{t} G\Big(W(s), s\Big)\, dW(s) \ . \tag{44}$$

For the discretization $t_0 < t_1 < t_2 < \cdots < t_{n+1} = t$, this integral is usually approximated by the sum

$$\mathrm{I}[G^{(n)}] = \sum_{i=1}^{n} G_i^{(n)}\ \Delta W_i \ , \tag{45}$$

where $G_i^{(n)} = G^{(n)}\Big(W(\tau_i), \tau_i\Big)$ with $\tau_i = t_i$ and the Wiener increment $\Delta W_i = W_{i+1} - W_i$ is given by (43). On should expect that the "random variable" $\mathrm{I}[G^{(n)}]$ has zero mean since it is a sum of random numbers ΔW_i with zero mean. However, to guarantee this, appropriate measurability conditions of the random function $G_i^{(n)}$ must imposed to ensure that $G_i^{(n)}$ and the Wiener increment ΔW_i are "independent",

$$\mathbb{E}\Big\{\, G_i^{(n)}\, \Delta W_i \,\Big\} = \mathbb{E}\Big\{\, G_i^{(n)} \,\Big\}\, \mathbb{E}\Big\{\, \Delta W_i \,\Big\} = 0 \tag{46}$$

which means, the nonanticipativeness of the integrand. The appropriate conditions, the mean-square convergence of the integrals $\mathrm{I}[G^{(n)}]$ to $\mathrm{I}[G]$ and the corresponding proofs are discussed

in great detail by Kloeden & Platen [23]. Here, we only cite some important results, for instance, the Itô isometry

$$\mathbb{E}\Big\{ \mathrm{I}[G] \Big\} = 0 \,, \tag{47}$$

$$\mathbb{E}\Big\{ \mathrm{I}^2[G] \Big\} = \int_{t_0}^{t} \mathbb{E}\Big\{ G^2\Big(W(s),s\Big) \Big\} ds \,, \tag{48}$$

$$\mathbb{E}\Big\{ \mathrm{I}[G]\,\mathrm{I}[H] \Big\} = \int_{t_0}^{t} \mathbb{E}\Big\{ G\Big(W(s),s\Big) H\Big(W(s),s\Big) \Big\} ds \,, \tag{49}$$

which may be immediately obtained by starting the computations from the approximate form of the Itô integral (45). A crucial point is the fact that the partial sums (45) depend on the particular choice of the intermediate point τ_i within an interval $[t_i,\, t_{i+1}]$ where the integrand $G\Big(W(\tau_i),\tau_i\Big)$ is evaluated. As mentioned above, for the choice $\tau_i = t_i$ the expression (45) define the Itô stochastic integral of the function G. This Itô interpretation and the corresponding calculus is used in this report. Another often useful choice of an intermediate point, namely, $\tau_i = (t_i + t_{i+1})/2$ leads to the Stratonovich interpretation, which satisfies the usual transformation rules of classical calculus. Note, that different interpretations lead to different solutions of the SDE which, however, can be related to each other [15, 23].

3.3. **Itô Formula.** In this sub-section we introduce the Itô formula and refer the reader for further details to the books of Gardiner and Kloeden & Platen [15, 23]. For this purpose, we consider the stochastical quantity $V(t)$ which obeys the SDE (39), where the coefficients F and B are now independent of W, and assume that the function Φ depends on this variable: $\Phi = \Phi(V,t)$. Then, the growth of Φ during the time step dt is given by the expansion

$$\begin{aligned} d\Phi(V,t) &= \Phi(V+dV, t+dt) - \Phi(V,t) \\ &= \dot{\Phi}(V,t)\,dt + \Phi'(V,t)\,dV + \frac{1}{2}\Phi''(V,t)\,dV^2 \,, \end{aligned} \tag{50}$$

where the dot and prime indicate the differentiation with respect to t and V, respectively. Since the Wiener increment (49) is proportional to $\sqrt{\Delta t}$, we also have to consider the second order term and get for the growth

$$\begin{aligned} d\Phi(V,t) &= \Big[\dot{\Phi} + \Phi'\,F(V,t) + \frac{1}{2}\Phi''\,B^2(V,t) \Big]\, dt \\ &+ \Phi'\,B(V,t)\,dW(t) \,, \end{aligned} \tag{51}$$

where we have applied that $\Big[dW(t)\Big]^2 = dt$, which is one of the key properties of the Itô calculus. The later relation is called Itô formula or stochastic chain rule and states that changing variables is not obtained by ordinary calculus (exception: Φ is linear in V), because of the appearence of the third term in the square braces of expression (51).

In order to obtain the multi-dimensional version of the Itô formula one has to start from the

multi-dimensional generalization of (39) which is given by

$$d\vec{V}(t) = \vec{F}(\vec{V},t)\,dt + \mathbb{B}(\vec{V},t)\,d\vec{W}(t)\;, \tag{52}$$

where $\vec{V}$, $\vec{F} \in \mathbb{R}^{\mathrm{d}}$ are d-dimensional vectors, the matrix $\mathbb{B} \in \mathbb{R}^{\mathrm{d}\times\mathrm{m}}$ is related to the diffusion tensor according to $\mathbb{D} = \mathbb{B}\mathbb{B}^T \in \mathbb{R}^{\mathrm{d}\times\mathrm{d}}$, and $\vec{W} \in \mathbb{R}^{\mathrm{m}}$ represents the m-dimensional Wiener process. Then, one can show that the growth of the function $\Phi = \Phi(\vec{V},t)$ has the form

$$\begin{aligned} d\Phi(\vec{V},t) &= \left\{ \frac{\partial\Phi}{\partial t} + \sum_p F_p(\vec{V},t)\frac{\partial\Phi}{\partial V_p} + \frac{1}{2}\sum_{p,q} D_{pq}(\vec{V},t)\frac{\partial^2\Phi}{\partial V_p\,\partial V_q}\right\} dt \\ &+ \sum_{p,q} B_{pq}(\vec{V},t)\frac{\partial\Phi}{\partial V_p}\,dW^q(t)\;, \end{aligned} \tag{53}$$

where D_{pq} and B_{pq} are the elements of $\mathbb{D}$ and $\mathbb{B}$, respectively. This equation establishes the multi-dimensional form of the Itô formula for multi-dimensional stochastic differentials with multi-dimensional Wiener processes

3.4. **Equivalence between the FP and SDE Approach.** In this sub-section we introduce the most attractive and important property, namely, the link between the FP equation and the SDE; see [15, 23] for further informations and stringent proofs. We consider the stochastic variable $\vec{V}(t)$ with the transition probability $P_2(\vec{V},t|\vec{V}_0,t_0)$, and assume that the arbirtary function $\psi(\vec{V},t)$ is twice continuously differentiable and vanishes at the boundary of the domain Ω. Applying the expectation value operator $\mathbb{E}$ to the Itô formula (53) for ψ, we obtain the expression

$$\begin{aligned} \frac{d}{dt}\mathbb{E}\Big\{\psi(\vec{V},t)\Big\} &= \mathbb{E}\Big\{\frac{\partial\psi}{\partial t}\Big\} + \sum_p \mathbb{E}\Big\{F_p(\vec{V},t)\,\frac{\partial\psi}{\partial V_p}\Big\} \\ &+ \frac{1}{2}\sum_{p,q}\mathbb{E}\Big\{D_{pq}(\vec{V},t)\,\frac{\partial^2\psi}{\partial V_p\,\partial V_q}\Big\}\;, \end{aligned} \tag{54}$$

where we already use the fact that the expectation of the last term of expression (54) vanishes

$$\mathbb{E}\Big\{B_{pq}\,\frac{\partial\psi}{\partial V_p}\,dW_q(t)\Big\} = 0$$

because of the nonanticipativeness requirement (46) and the result that $\mathbb{E}\{dW_q(t)\} = 0$. Using for the expectation the expression $\mathbb{E}\{(...)\} = \int\limits_\Omega d^3V\,P_2(\vec{V},t|\vec{V}_0,t_0)\,(...)$, keeping in mind the imposed properties on ψ and performing integration by parts we get the result

$$\int\limits_\Omega d^3V\,\psi(\vec{V},t)\left\{\frac{\partial P_2}{\partial t} + \sum_p \frac{\partial}{\partial V_p}\Big[F_p\,P_2\Big] - \frac{1}{2}\sum_{p,q}\frac{\partial^2}{\partial V_p\partial V_q}\Big[D_{pq}\,P_2\Big]\right\} = 0\;. \tag{55}$$

Clearly, because ψ is an arbitrary function, the expression in the curly braces must be zero, yielding the FP equation

$$\frac{\partial P_2}{\partial t} = -\sum_p \frac{\partial}{\partial V_p}\Big[F_p\,P_2\Big] + \frac{1}{2}\sum_{p,q}\frac{\partial^2}{\partial V_p\partial V_q}\Big[D_{pq}\,P_2\Big] \tag{56}$$

for the transition probability P_2 of the variable $\vec{V}$. Obviously, we recognize the complete equivalence between the SDE (52) and the diffusion process – described by the FP equation

(56) – which is defined by the drift coefficients $F_p(\vec{V},t)$ and diffusion coefficients $D_{pq}(\vec{V},t)$ (cf. equations (25)-(27)). This equivalence will be exploit in the following: instead to solve the FP equation (2) for the distribution function f_α of the particle specie "α", we solve numerically the corresponding SDE (52) for the particles of this ensemble. Due to this close connection, the small-angle electron-electron collisions will be treated by the solution of a Langevin-type SDE and, consequently, fits in a natural way into the PIC method, which is one basic concept of the hybrib PIC/DSMC code development [2].

3.5. **Itô-Taylor Expansion.** In contrast to the Taylor expansion for the function $f:\mathbb{R}\to\mathbb{R}$ of a deterministic variable X, we expect a more complicated series expansion for a stochastic variable V due to the modified chain rule in Itô calculus (see, relations (51) and (53)). The stochastic counterpart of the deterministic Taylor formula for the expansion of a smooth function is, especially, important for the derivation of numerical methods for SDEs. There are several posibilities to introduce stochastic Taylor series expansion (see, for instance [20, 23]), which is called "Itô-Taylor Expansion" (ITE) in the following. In the context of the present report the ITE is obtained by iterated application of the Itô formula (51) in one dimension or (53) in the multi-dimensional case; more details about this proceeding is found in the books [23, 24]. The integration of the multi-dimensional Itô formula (53) for the function $f:\mathbb{R}^d\to\mathbb{R}$ yields

$$f\{\tau\} = f\{t_0\} + \int_{t_0}^{\tau} ds \left[\mathcal{L}^{(0)} f\right]\{s\} + \sum_{q=1}^{m} \int_{t_0}^{\tau} dW_s^q \left[\mathcal{L}^{(q)} f\right]\{s\}\,, \tag{57}$$

where the operators $\mathcal{L}^{(0)}$ and $\mathcal{L}^{(j)}$ are defined by

$$\mathcal{L}^{(0)} f = \left\{ \frac{\partial}{\partial t} + \sum_{j=1}^{d} F_j \frac{\partial}{\partial V_j} + \frac{1}{2} \sum_{j,k=1}^{d} D_{jk} \frac{\partial^2}{\partial V_j\, \partial V_k} \right\} f \tag{58}$$

and

$$\mathcal{L}^{(q)} f = \left\{ \sum_{j=1}^{d} B_{jq} \frac{\partial}{\partial V_j} \right\} f\,, \tag{59}$$

respectively, and $\{t\}$ abbreviates $\{t\} = \left(\vec{V}(t),\, t\right)$. To obtain the multi-dimensional ITE of the variable $\vec{V}(t)$, we integrate the SDE (52) over $[t_0,\, t = t_0 + \tau]$, use equation (57) for $f = F_i$

and $f = B_{iq}$, respectively, and get after some rearrangements the expression

$$\begin{aligned} V_i(t) &= V_i(t_0) \\ &+ F_i\{t_0\} \int_{t_0}^{t} ds_2 + \int_{t_0}^{t} ds_2 \int_{t_0}^{s_2} ds_1 \Big[\mathcal{L}^{(0)}\, F_i\Big]\{s_1\} \\ &+ \sum_{q=1}^{m} \int_{t_0}^{t} ds_2 \int_{t_0}^{s_2} dW_{s_1}^q \Big[\mathcal{L}^{(q)}\, F_i\Big]\{s_1\} \\ &+ \sum_{q=1}^{m} B_{iq}\{t_0\} \int_{t_0}^{t} dW_{s_2}^q + \sum_{q=1}^{m} \int_{t_0}^{t} dW_{s_2}^q \int_{t_0}^{s_2} ds_1 \Big[\mathcal{L}^{(0)}\, B_{iq}\Big]\{s_1\} \\ &+ \sum_{p,q=1}^{m} \int_{t_0}^{t} dW_{s_2}^q \int_{t_0}^{s_2} dW_{s_1}^p \Big[\mathcal{L}^{(p)}\, B_{iq}\Big]\{s_1\} \end{aligned} \tag{60}$$

for the i^{th} component of $\vec{V} \in \mathbb{R}^d$. In order to simplify the presentation, we define the multiple Itô integral of the function f according to

$$\begin{aligned} \mathrm{I}_{(j_1,j_2,\ldots,j_l);\,t_0,t}\big[f\big] &= \int_{t_0}^{t} \int_{t_0}^{s_l} \ldots \int_{t_0}^{s_2} f(s_1)\, dW_{s_1}^{j_1} \ldots dW_{s_{l-1}}^{j_{l-1}}\, dW_{s_l}^{j_l} \\ &= \int_{t_0}^{t} dW_{s_l}^{j_l} \int_{t_0}^{s_l} dW_{s_{l-1}}^{j_{l-1}} \ldots \int_{s_2}^{t} dW_{s_1}^{j_1}\, f(s_1)\ , \end{aligned} \tag{61}$$

with $j_i \in \{0, 1, \ldots, m\}$ for $i \in \{1, 2, \ldots, l\}$ and $m = 1, 2, \ldots$, where it is assumed that $dW_s^0 = ds$ [2]. Obviously, from (60) we recognize that multiple stochastic integrals are central building blocks for the representation of the approximate solution of the SDE (52). With the additional abbreviation $\mathrm{I}_{(j_1,j_2,\ldots,j_l)} = \mathrm{I}_{(j_1,j_2,\ldots,j_l);\,t_0,t}\big[1\big]$, we immediately can express the terms including only multiplicity one Itô integral. These are

$$F_i\{t_0\} \int_{t_0}^{t} ds_2 = F_i\{t_0\}\, \mathrm{I}_{(0)} \tag{62}$$

and

$$\sum_{q=1}^{m} B_{iq}\{t_0\} \int_{t_0}^{t} dW_{s_2}^q = \sum_{q=1}^{m} B_{iq}\{t_0\}\, \mathrm{I}_{(q)}\ . \tag{63}$$

For our purposes it is enough (for the moment) to consider a stochastic Taylor expansion up to first order in τ. Because $ds \sim \tau$ and $dW_s^j \sim \tau^{1/2}$, a closer inspection of relation (60) reveals that besides the terms (62) and (63) only the last term on the rhs of (60) contributes to a first order stochastic Taylor expansion. Inserting $f = \mathcal{L}^{(p)}\, B_{iq}$ into (57) and using definition

[2] Note, that for f=1 and $j_1 = j_2 = \cdots = j_l$ the Itô integral (61) can be expressed according to $\mathrm{I}_{(j,j,\ldots,j);\,t_0,t} = \frac{1}{l!}\Big(\frac{t-t_0}{2}\Big)^{l/2} \mathrm{H}_l\Big(\frac{W_t^j - W_{t_0}^j}{\sqrt{2(t-t_0)}}\Big)$, where $\mathrm{H}_l(z) = (-1)^l \mathrm{e}^{z^2} \frac{d^l}{dz^l} \mathrm{e}^{-z^2}$ are the Hermite polynomials.

(61) yields

$$\sum_{p,q=1}^{m} \int_{t_0}^{t} dW_{s_2}^{q} \int_{t_0}^{s_2} dW_{s_1}^{p} \Big[\mathcal{L}^{(p)}\, B_{iq}\Big]\{s_1\} = \sum_{p,q=1}^{m} \Big[\mathcal{L}^{(p)}\, B_{iq}\Big]\{t_0\}\, \mathrm{I}_{(p,q)} \tag{64}$$

for the last term on the rhs of (60) up to first order. Then, the final expression of the first order ITE for the stochastic variable $\vec{V}(t)$ reads as

$$\begin{aligned} V_i(t) &= V_i(t_0) + F_i\{t_0\}\, \mathrm{I}_{(0)} + \sum_{q=1}^{m} B_{iq}\{t_0\}\, \mathrm{I}_{(q)} \\ &+ \sum_{p,q=1}^{m} \Big[\mathcal{L}^{(p)}\, B_{iq}\Big]\{t_0\}\, \mathrm{I}_{(p,q)} + \mathrm{R}\Big(\mathcal{O}(\tau^{3/2})\Big)\,, \end{aligned} \tag{65}$$

where the remainder is given by

$$\begin{aligned} \mathrm{R}\Big(\mathcal{O}(\tau^{3/2})\Big) &= \sum_{q=1}^{m} \int_{t_0}^{t} ds_2 \int_{t_0}^{s_2} dW_{s_1}^{q} \Big[\mathcal{L}^{(q)}\, F_i\Big]\{s_1\} \\ &+ \sum_{q=1}^{m} \int_{t_0}^{t} dW_{s_2}^{q} \int_{t_0}^{s_2} ds_1 \Big[\mathcal{L}^{(0)}\, B_{iq}\Big]\{s_1\} \\ &+ \sum_{p,q,r=1}^{m} \int_{t_0}^{t} dW_{s_3}^{q} \int_{t_0}^{s_3} dW_{s_2}^{p} \int_{t_0}^{s_2} dW_{s_1}^{r} \Big[\mathcal{L}^{(r)}\, \mathcal{L}^{(p)}\, B_{iq}\Big]\{s_1\} \\ &+ \sum_{p,q=1}^{m} \int_{t_0}^{t} dW_{s_3}^{q} \int_{t_0}^{s_3} dW_{s_2}^{p} \int_{t_0}^{s_2} ds_1 \Big[\mathcal{L}^{(0)}\, \mathcal{L}^{(p)}\, B_{iq}\Big]\{s_1\} \\ &+ \int_{t_0}^{t} ds_2 \int_{t_0}^{s_2} ds_1 \Big[\mathcal{L}^{(0)}\, F_i\Big]\,. \end{aligned} \tag{66}$$

Note, that the first three terms on the rhs of the latter expression vanish at least with $\mathcal{O}(\tau^{3/2})$ while the last two terms vanishes at least with $\mathcal{O}(\tau^2)$ when τ tends to zero.

3.6. **Explicit Strong Itô-Taylor Schemes.** Based on the previous sub-section, we present here schemes for the numerical solution of SDEs, where we follow the textbooks of [23, 24]. In general, the numerical solution of SDEs requires to determine random numbers and the schemes are classified in weak and strong convergence approximations. If these random variables only have to coincide in their lower order moments with those of – for instance – Gaussian random numbers to provide an accurate approximation, the corresponding schemes are called weak convergence approximations. Unfortunately, a clear (and stringent) distinction between the weak and strong approximation of a SDE is seldom found in the literature [20, 27, 41, 1], and, therefore further investigations should decide whether weak approximations are suitable in the scope of electron-electron collision modeling. In the context of the present report, we apply strong Taylor schemes to approximate the solution of the SDEs with respect to the strong convergence criterion. Roughly speaking, this kind of approximation needs in a certain sense the resolution of the "inner structure" of the random variables, which is much more

difficult to achieve than the agreement with lower order moments (see below).

One-Dimensional Schemes ($d = m = 1$): The simplest strong Taylor approximation of the SDE (39), is the Euler scheme of the form ($\Delta t_n = \tau$)

$$C^{\,n+1} = C^{\,n} + F\Big(C^{\,n}, t_n\Big)\,\Delta t_n + B\Big(C^{\,n}, t_n\Big)\,\sqrt{\Delta t_n}\,\eta_n\;, \tag{67}$$

for the approximation $C(t)$ of the stochastic variable $V(t)$, where $C^{\,n} = C(t_n)$ and $C_0 = V(t_0)$. It is obvious from the ITE that this scheme contains only Wiener integrals of multiplicity one, which are given by $\mathrm{I}_{(0)} = \Delta t_n$ and $\mathrm{I}_{(1)} = \Delta W_n = \sqrt{\Delta t_n}\,\eta_{n+1}$ (see relation (43)), respectively, where $\eta_{n+1} \sim \mathcal{N}(0,1)$ is a Gaussian distributed random number with mean $\mu = 0$ and variance $\sigma^2 = 1$. Note, that the Euler scheme converges with strong order $\gamma = 1/2$. The order of the Euler scheme can easily be improved by considering the next term of the ITE (65), which is given by $B\,\frac{dB}{dC}\,\mathrm{I}_{(1,1)}$ with $\mathrm{I}_{(1,1)} = \int\limits_{t_0}^{t} dW_{s_2} \int\limits_{t_0}^{s_2} dW_{s_1}$. The Itô integral $\mathrm{I}_{(1,1)}$ of multiplicity two can be computed analytically (see footnote 2) and approximated with (43) according to

$$\mathrm{I}_{(1,1)} = \frac{1}{2}\Big[(W_{t+\Delta t} - W_t)^2 - \Delta t\Big] \approx \frac{1}{2}\Big[(\Delta W_n)^2 - \Delta t_n\Big]\;. \tag{68}$$

Finally, the Taylor scheme of strong order $\gamma = 1$ reads as

$$\begin{aligned} C^{\,n+1} &= C^{\,n} + F\Big(C^{\,n}, t_n\Big)\,\Delta t_n + B\Big(C^{\,n}, t_n\Big)\,\Delta W_n \\ &+ \frac{1}{2}B\,B'\,\Big[(\Delta W_n)^2 - \Delta t_n\Big]\;, \end{aligned} \tag{69}$$

which was first proposed by Milstein, where $\Delta W_n = \sqrt{\Delta t_n}\,\eta_{n+1}$ and $B' = dB/dC$. Clearly, the latter equation reveals a certain disadvantage of the strong Taylor approximation, namely, the derivative of the diffusion coefficient $B = \sqrt{D}$ must be evaluated. Note, that in the general case, the derivatives of various orders of the diffusion and drift coefficients have to be considered. Strong schemes which avoid the computation of derivatives at each time step are known as explicit strong approximations. To obtain the explicit Milstein scheme we consider

$$B\Big(C^{\,n} + \Delta C^{\,n}\Big) - B\Big(C^{\,n}\Big) = \Big[F\Big(C^{\,n}\Big)\,\Delta t_n + B\Big(C^{\,n}\Big)\,\sqrt{\Delta t_n}\Big]B' \;\approx \sqrt{\Delta t_n}\,B\,B'\;,$$

and get in the lowest order of this approximation the explicit strong order $\gamma = 1$ scheme due to Platen

$$\begin{aligned} C^{\,n+1} &= C^{\,n} + F\Big(C^{\,n}, t_n\Big)\,\Delta t_n + B\Big(C^{\,n}, t_n\Big)\,\Delta W_n \\ &+ \frac{1}{2\sqrt{\Delta t_n}}\Big[B\Big(\tilde{C}^{\,n}, t_n\Big) - B\Big(C^{\,n}, t_n\Big)\Big]\,\Big[(\Delta W_n)^2 - \Delta t_n\Big]\;, \end{aligned} \tag{70}$$

with the supporting value

$$\tilde{C}^{\,n} = C^{\,n} + F\Big(C^{\,n}, t_n\Big)\,\Delta t_n + B\Big(C^{\,n}, t_n\Big)\,\sqrt{\Delta t_n}\;, \tag{71}$$

where $\Delta W_n = \sqrt{\Delta t_n}\,\eta_{n+1}$ with $\eta_{n+1} \sim \mathcal{N}(0,1)$.

Multi-Dimensional Schemes: In the following we present strong Taylor approximations for the

multi-dimensional SDE (52). In order to find the lowest strong order schemes in vector form, we first introduce the auxilary vector

$$\vec{b}_p^{\,n} = \mathbb{B}\Big(\vec{C}^{\,n}, t_n\Big)\,\vec{e}_p \in \mathbb{R}^d \tag{72}$$

at the time level t_n, which represents the p$^{\text{th}}$ column of the matrix $\mathbb{B}$, and $\vec{e}_p \in \mathbb{R}^m$ is a unit vector with the entry "1" in the p$^{\text{th}}$ row. Then, for the approximation $\vec{C}(t)$ of the stochastic variable $\vec{V}(t)$, we obtain from the ITE (65)

$$\begin{aligned}\vec{C}^{\,n+1} &= \vec{C}^{\,n} + \vec{F}\Big(\vec{C}^{\,n}, t_n\Big)\,\mathrm{I}_{(0)} + \sum_{q=1}^{m} \vec{b}_q^{\,n}\,\mathrm{I}_{(q)} \\ &+ \sum_{p,q=1}^{m} \vec{b}_p^{\,n} \cdot \nabla_c\, \vec{b}_q^{\,n}\,\mathrm{I}_{(p,q)} + \mathcal{O}(\Delta t^{3/2})\,,\end{aligned} \tag{73}$$

where we used the result that $\mathcal{L}^{(p)}$ can be expressed by

$$\mathcal{L}^{(p)} = \vec{b}_p^{\,n} \cdot \nabla_c$$

with the nabla operator $\nabla_c = \left(\frac{\partial}{\partial C_1}, \frac{\partial}{\partial C_2}, \frac{\partial}{\partial C_3}\right)^T$. Considering only the first three terms of the rhs (73), we obtain the forward Euler scheme of strong order $\gamma = 1/2$. Including the remaining term, expression (73) establish the stong $\gamma = 1$ order Milstein scheme, where the analytical form of the diffusion coefficients are needed to perform the derivatives. The explict – which means derivation free – strong Milstein scheme in the multi-dimensional case is obtained by replacing the derivation according to

$$\vec{b}_p^{\,n} \cdot \nabla_c\, b_{q,i}^n = \frac{1}{\sqrt{\Delta t_n}}\Big[b_{q,i}^n\big(\vec{S}_p^n\big) - b_{q,i}^n\big(\vec{C}^n\big)\Big] \tag{74}$$

with the supporting vector

$$\vec{S}_p^n = \vec{C}^n + \Delta\vec{C}^n\,; \quad \Delta\vec{C}^n = \vec{F}\Big(\vec{C}^{\,n}, t_n\Big)\,\Delta t_n + \vec{b}_p^{\,n}\,\sqrt{\Delta t_n}\,, \tag{75}$$

where $b_{q,i}^n$ is the i$^{\text{th}}$ component of $\vec{b}_q^{\,n}$. Similar to the one-dimensional case, the Itô integrals of multiplicity one are approximated according to $\mathrm{I}_{(q)} = \Delta W_n^q = \sqrt{\Delta t_n}\,\eta_{n+1}^q$ with $\eta_{n+1}^q \sim \mathcal{N}(0,1)$. However, an additional difficulty arise in computing the Itô integrals of multiplicity two. In order to evaluate these integral, we adopt from the literature the result

$$\mathrm{I}_{(p,q)} = \begin{cases} \frac{1}{2}\Big[\Big(\Delta W_n^p\Big)^2 - \Delta t_n\Big] & \text{for } p = q \\ \mathrm{J}_{(p,q)} & \text{for } p \neq q \end{cases}, \tag{76}$$

which allows to compute the Itô integral $\mathrm{I}_{(p,q)}$ from its Stratonovich counterpart $\mathrm{J}_{(p,q)}$. It is possible to represent multiple stochastic Stratonovich integrals in effectiv approximate way. The method for multiple Stratonovich integrals based on the Fourier (Kahunen-Loéwe) series expansion; for details we refer the reader to the books [24] or [23]. In essence, the series expansion is truncated at P_S and the multiple Stratonovich integrals $\mathrm{J}_{(j_1,j_2,\ldots,j_l);\,\Delta t}$ are approximated by Riemann-Stieltjes integrals $\mathrm{J}^{(P_S)}_{(j_1,j_2,\ldots,j_l);\,\Delta t}$, which converge to the Stratonovich

integral. After a simple, but lengthy computation we obtain the result (see also Appendix G)

$$\begin{aligned} \mathrm{J}_{(p,q)}^{(P_S)} &= \frac{\Delta t}{2}\,\xi_p\,\xi_q + \Delta t\,\sqrt{\rho_{P_S}}\left(\mu_p^{(P_S)}\,\xi_q - \mu_q^{(P_S)}\,\xi_p\right) \\ &+ \frac{\Delta t}{2\pi}\sum_{r=1}^{P_S}\frac{1}{r}\left[\zeta_{p,r}\left(\sqrt{2}\,\xi_q + \eta_{q,r}\right) - \zeta_{q,r}\left(\sqrt{2}\,\xi_p + \eta_{p,r}\right)\right] \end{aligned} \tag{77}$$

with

$$\rho_{P_S} = \frac{1}{12} - \frac{1}{2\pi^2}\sum_{r=1}^{P_S}\frac{1}{r^2}\,, \tag{78}$$

where ξ_j, $\zeta_{j,k}$, $\eta_{j,k}$ and $\mu_j^{(P_S)}$ are independent standard Gaussian random variables (which means, zero mean and variance one: $\mathcal{N}(0,1)$). It is obvious from the latter expression that the strong Milstein scheme is numerical much more expensive than the strong forward Euler, because a lot of additional random variables have to be generated. Furthermore, if we interpret Itô integrals as random numbers, it is clear from equation (77) that, especially high multiplicity integrals possess a very complex "inner structure" which may be resolved by standard Gaussian random numbers.

Numerical Experiment: In order to investigate the approximation behavior of the strong forward Euler and Milstein scheme (73) experimentally, we consider the one-dimensional Itô process $V = \left\{V(t)\,; 0 = t_0 \le t \le T = 1\right\}$ satisfying

$$dV(t) = -\frac{1}{2}\,V(t)\,dt + V(t)\,dW^1(t) + V(t)\,dW^2(t) \tag{79}$$

on the time interval $0 \le t \le 1$ for the initial value $V_0 = V(0) = 1$, where $W^1(t)$ and $W^2(t)$ are two independent Wiener processes. Using the multi-dimensional Itô formula (53) for $\Phi = \ln V(t)$, we can immediately check that the SDE (79) has the analytical solution

$$V(t) = V_0 \exp\left\{-\frac{3}{2}\,t + W^1(t) + W^2(t)\right\}\,, \tag{80}$$

where $\Delta W^j(t)$ is determined from relation (42). For the comparison of the strong approximation of the SDE (79) according to (73) with the analytical solution (80), we organized the simulation into $M = 40$ batches of $N = 100$ trajectories each and compute the mean $\hat{\epsilon}$ of the batch average $\hat{\epsilon}_k$ from

$$\hat{\epsilon} = \frac{1}{M}\sum_{k=1}^{M}\hat{\epsilon}_k = \frac{1}{M}\sum_{k=1}^{M}\left(\frac{1}{N}\sum_{j=1}^{N}\left|V_{j,k}(T) - C_{j,k}(T)\right|\right) \tag{81}$$

for different discretizations $\Delta t = 2^{-n}$ of the considered time interval, where $C_{j,k}(T)$ represents the solution of the strong Euler or Milstein approximation. The results depicted in Figure 3.1, where the mean of the batch averages $\hat{\epsilon}$ is plotted as a function of the discretization exponent n for the Euler (full line with gradients), the Milstein (full line with squares; $P_S = \min(2^n,\,512)$) and the derivation-free Milstein (dashed-dotted line with open circles; $P_S = 16$) scheme. Clearly, this plot demonstrate that the agreement between the Milstein scheme with and without derivations is very good and suggests to use the less expensive derivation-free scheme. Furthermore, we derive from the slope of the curves that the experimental order of convergence

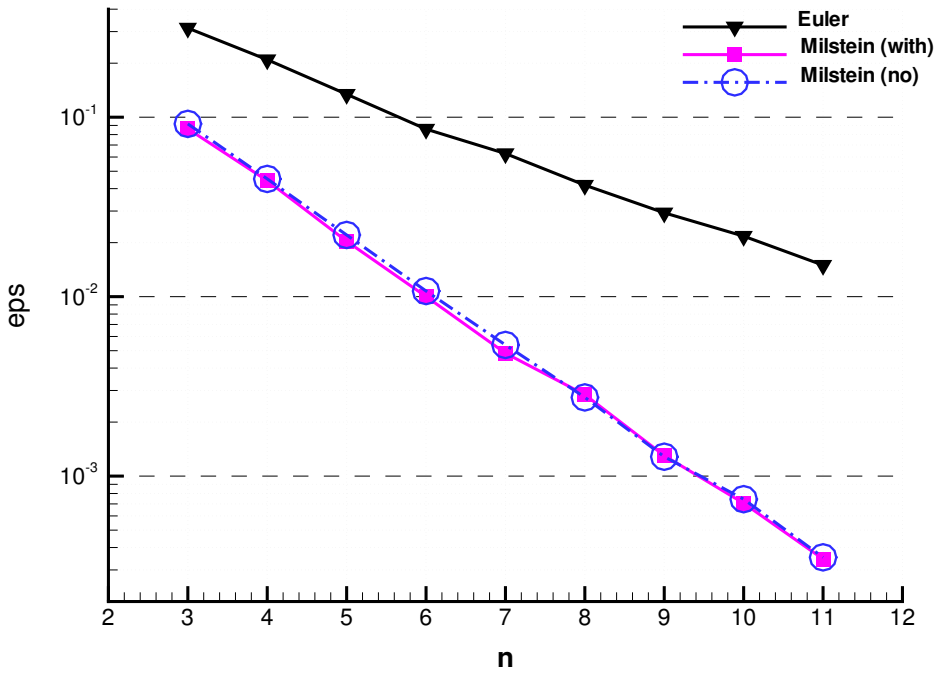

FIGURE 3.1. Comparison of the mean batch average $\hat{\epsilon}$ (= eps) as a function of the exponent n (corresponding to the discretization $\Delta t = 2^{-n}$) for the Euler scheme (full line with gradients), the Milstein scheme with derivations (full line with squares; $P_S = \min(2^n, 512)$) and the derivation-free Milstein scheme (dashed-dotted line with open circles; $P_S = 16$).

is $\sim$ 0.54 and $\sim$ 1.01 for the Euler and the Milstein scheme, respectively, which agree very well with the nominal strong order of $\gamma = 1/2$ and $\gamma = 1$. Finally note, that $\hat{\epsilon}$ may be considered as a (statistically) measure of the pathwise closeness at the end of the time interval $[0, 1]$, which represent the absolute error criterion. Moreover, the quality of the estimate (81) can be assessed with the variance

$$\hat{\sigma}_\epsilon^2 = \frac{1}{M-1} \sum_{k=1}^{M} \left(\hat{\epsilon}_k - \hat{\epsilon} \right)^2$$

of the batch averages, which is necessary to evaluate a confidence interval for $\hat{\epsilon}$ based on the Student t-distribution [24].

4. Numerical Framework: PIC in Velocity Space

The key quantities to solve the Langevin-type differential equation are the velocity dependent friction (3) and diffusion (4) coefficients at each time step $t = t_n$. For this purpose a PIC-type, self-consistent numerical scheme is constructed in the velocity space. Schematically a typical PIC-cycle is depicted in Figure 4.1. The peculiarity of this PIC scheme [19, 4] is the fact that it is built in the velocity space, and then classically divided in two areas, one mesh-free and one grid-based. In the following the different building blocks of the PIC scheme are discussed in detail. For sake of clearness, we consider here a single grid cell of the spatial com-

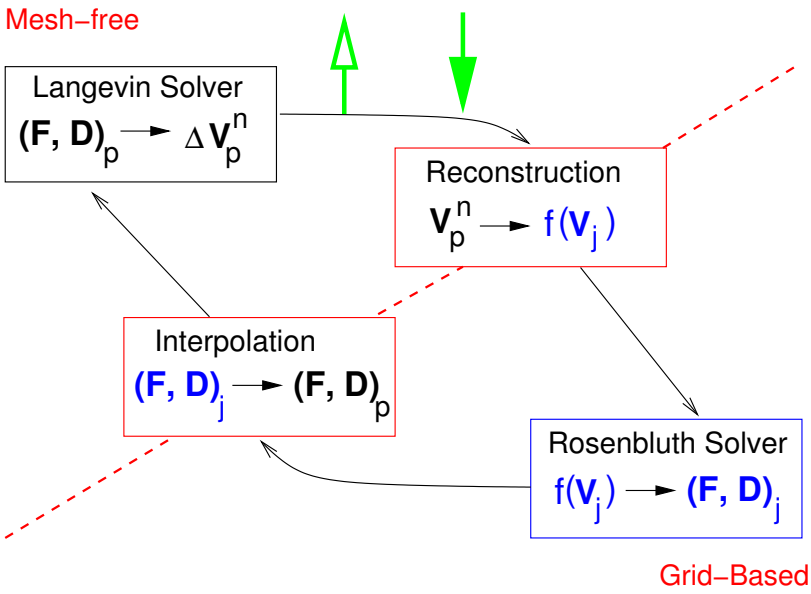

Figure 4.1. Schematical description of the Fokker-Planck solver based on the PIC method in the velocity space.

putational domain, containing a sufficient large number of particles (of a certain specie "α"). Furthermore, if it is skilful and pedagogical sensible we will introduce the three-dimensional formulation of the numerical schemes, else we switch to lower-dimensional descriptions which could be straightforward generalized.

Associated with each local grid zone is a Cartesian mesh in velocity space with an equidistant spacing Δu, Δv and Δw in $x-$, $y-$, and $z-$direction, respectively, which is built up according to

$$\begin{aligned} u_{i,j,k} &= u_0 + (i-1)\,\Delta u\,, \quad 1 \le i \le I+1 \\ v_{i,j,k} &= v_0 + (j-1)\,\Delta v\,, \quad 1 \le j \le J+1 \\ w_{i,j,k} &= w_0 + (k-1)\,\Delta w\,, \quad 1 \le k \le K+1\,. \end{aligned} \tag{82}$$

Here, u, v, and w are the components of the velocity grid vector $\vec{v}_{i,j,k} = \Big(u,\, v,\, w\Big)^T_{i,j,k}$ and $\Big(u_0,\, v_0,\, w_0\Big)^T$ are the coordinates of the starting point of the velocity grid.

Reconstruction Block (Localization and Assignment). From the actual location of the plasma particles in mesh-free velocity space, the distribution function $f(\mathbf{c})$ is constructed on the Cartesian velocity mesh in two steps. At first the particles have to be located with respect

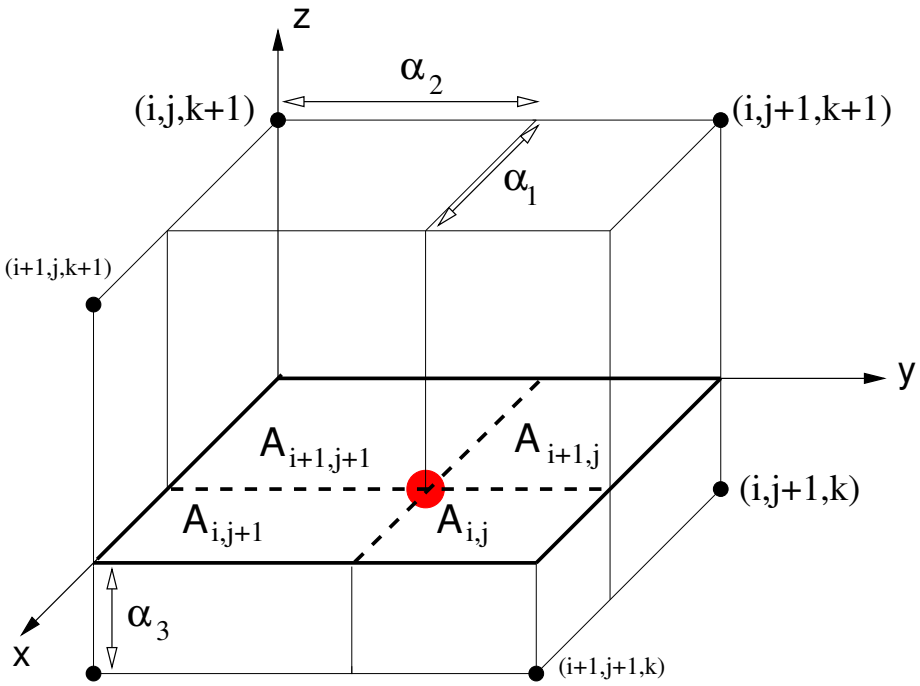

FIGURE 4.2. Assignment of the particle's velocity to the nodes (grid-based model) and interpolation of the results obtained in the nodes onto the particle's position in velocity space (mesh-free model) with the aid of the volume-weighting approach.

to the velocity grid. To identify the adress of the cell $Z_{i,j,k}$ where the particle's velocity is found, we apply the localization strategy

$$\begin{aligned} i_p &= \frac{1}{\Delta u}\mathrm{INT}\Big([V_1]^n_p - u_0\Big) + 1 \\ j_p &= \frac{1}{\Delta v}\mathrm{INT}\Big([V_2]^n_p - v_0\Big) + 1 \\ k_p &= \frac{1}{\Delta w}\mathrm{INT}\Big([V_3]^n_p - w_0\Big) + 1\,, \end{aligned} \tag{83}$$

where $\vec{V}^n_p = \Big([V_1]^n_p,\, [V_2]^n_p,\, [V_3]^n_p\Big)^T$ is the velocity vector of the p^{th} particle at time t_n and INT(.) denotes the integer part of a real number. Note, that the strength – namely, the high efficiency – of this approach is a consequence of the equidistant grid spacing. Secondly, after the particle is localized in the grid cell Z_{i_p,j_p,k_p} of the velocity mesh, we have to bridge

the gap between the mesh-free and grid-based computations. For this purpose, we introduce the relative weighting coordinates $\vec{\alpha}^{(p)} = \left(\alpha_1^{(p)}, \alpha_2^{(p)}, \alpha_3^{(p)}, \right)$ of the p$^{\text{th}}$ particle at $t = t_n$ according to

$$\begin{aligned} \alpha_1^{(p)} &= \frac{1}{\Delta u}\left([V_1]_p^n - u_{i_p,j_p,k_p}\right) \\ \alpha_2^{(p)} &= \frac{1}{\Delta v}\left([V_2]_p^n - v_{i_p,j_p,k_p}\right) \\ \alpha_3^{(p)} &= \frac{1}{\Delta w}\left([V_3]_p^n - w_{i_p,j_p,k_p}\right) . \end{aligned} \tag{84}$$

It is obvious, that the weights $g_{i,j,k}^{(p)}$ of the considered particle have to be calculated with respect to the surrounding eight nodes of the grid (see Figure 4.2). The first step to do this, is to compute the four areas of the section parallel to the (x, y)-plane, where the particle is located. According to the area-weighting method [30, 19] we get

$$\begin{aligned} A_{i,j} &= \left(1 - \alpha_1^{(p)}\right)\left(1 - \alpha_2^{(p)}\right) \\ A_{i+1,j} &= \alpha_1^{(p)}\left(1 - \alpha_2^{(p)}\right) \\ A_{i,j+1} &= \left(1 - \alpha_1^{(p)}\right)\alpha_2^{(p)} \\ A_{i+1,j+1} &= \alpha_1^{(p)}\,\alpha_2^{(p)} . \end{aligned} \tag{85}$$

These areas form the bases of eight cuboids

$$\begin{aligned} \begin{matrix} g_{i,j,k}^{(p)} \\ g_{i,j,k+1}^{(p)} \end{matrix} &= A_{i,j} \begin{cases} 1 - \alpha_3^{(p)} \\ \alpha_3^{(p)} \end{cases} \\ \begin{matrix} g_{i+1,j,k}^{(p)} \\ g_{i+1,j,k+1}^{(p)} \end{matrix} &= A_{i+1,j} \begin{cases} 1 - \alpha_3^{(p)} \\ \alpha_3^{(p)} \end{cases} \\ \begin{matrix} g_{i,j+1,k}^{(p)} \\ g_{i,j+1,k+1}^{(p)} \end{matrix} &= A_{i,j+1} \begin{cases} 1 - \alpha_3^{(p)} \\ \alpha_3^{(p)} \end{cases} \\ \begin{matrix} g_{i+1,j+1,k}^{(p)} \\ g_{i+1,j+1,k+1}^{(p)} \end{matrix} &= A_{i+1,j+1} \begin{cases} 1 - \alpha_3^{(p)} \\ \alpha_3^{(p)} \end{cases} . \end{aligned} \tag{86}$$

which represent the relative coordinates $\vec{\alpha}^{(p)}$ depending weights of the p$^{\text{th}}$ particle located in the grid cell Z_{i_p,j_p,k_p}. As one would expect, the weights fulfil the relation

$$\sum_{\mu,\nu\lambda=0}^{1} g_{i+\mu,j+\nu,k+\lambda}^{(p)} = 1 , \tag{87}$$

and, obviously can be interpreted as fraction of the volume of the actual grid cell. Furthermore, the applied method may be considered as an extension of the well-known area-weighting method to three dimensions and, hence will be called volume-weighting technique.

Rosenbluth Solver. The reconstructed field particle (scatterer) distribution function on the velocity grid is used for the computation of the Rosenbluth potentials and their derivatives,

from which the friction and diffusion coefficients for the test particles are determined. In order to be free of any model assumption – like isotropic distribution of the field particles –, we apply Discrete Fourier Transformation (DFT) techniques [7, 6, 41]. As it is discussed in detail by Brigham [7], the DFT represents a special case of the (continuous) Fourier integral transformation, to which three "modifications" are necessary. The DFT in one dimension may be defined according to

$$f_\tau = \frac{1}{N} \sum_{\sigma=0}^{N-1} \hat{f}_\sigma \, \mathrm{e}^{2\pi i \frac{\tau\sigma}{N}} \; ; \quad \tau = 0, 1, \ldots, N-1 \tag{88}$$

and

$$\hat{f}_\sigma = \sum_{\tau=0}^{N-1} f_\tau \, \mathrm{e}^{-2\pi i \frac{\tau\sigma}{N}} \; ; \quad \sigma = 0, 1, \ldots, N-1 \, , \tag{89}$$

where the signal f_τ in **c**-space and the spectrum $\hat{f}_\sigma$ in **k**-space form a discrete transform pair indicated by $f_\tau \Leftrightarrow \hat{f}_\sigma$ [3]. The application of the DFT implicitly requires a periodicity of the discrete signal and spectrum

$$f_\tau = f_{\tau+mN} \quad \text{and} \quad \hat{f}_\sigma = \hat{f}_{\sigma+mN} \; ; \quad m = 0, \pm 1, \pm 2, \ldots \; , \tag{90}$$

which means, that the N sampling values of both representing one period of a periodic (discrete) function. Instead to apply directly the discrete convolution to the integrals (6) and (7), we use the DFT to get an approximation of the Fourier transform $\hat{f}_{scat}(k_s) = \int_{-\infty}^{\infty} dc_s \, \mathrm{e}^{-2\pi i c_s k_s} \, f_{scat}(c_s)$ of the field particle distribution $f_{scat}(c_s)$, where the quality of this approximation depends strongly on the shape of the signal under consideration (cf., [7]). According to the relations (8) - (11), multiplications are performed in **k**-space to obtain the Fourier transforms of the Rosenbluth potentials and their derivatives. Afterwards, the DFT is applied once again for the approximation of the inverse Fourier transforms from which the friction (3) and diffusion (4) coefficients are computed in velocity space.

Numerical and Algorithmical Aspects of the FFT. A fast Fourier transform (FFT) is an efficient algorithm to compute the DFT and its inverse. FFTs are of great importance to a wide variety of applications, from digital signal processing to solving partial differential equations to algorithms for quickly multiplying large integers [38]. The DFT is defined by the formula (89) and can be rewritten as

$$F_n = \sum_{k=0}^{N-1} W^{n\,k} \, f_k \; ; \quad n = 0, 1, \ldots, N-1 \quad \Longleftrightarrow \quad \vec{F} = \mathbb{W} \vec{f} \tag{91}$$

where the complex number W is given by

$$W = \mathrm{e}^{-2\pi i/N} \tag{92}$$

and $\hat{f}_n$ is replaced by F_n for convenience. In other words, the vector $\vec{f}$ is multiplied by a matrix $\mathbb{W}$, whose (n, k)-th element is the constant W to the power $n \cdot k$, yielding the vector $\vec{F}$

[3] Note, the comparison with the continuous Fourier transformations requires a scaling with K_s and C_s, respectively, which are the constant sampling intervals in **k**- and **c**-space.

with components F_n. This matrix multiplication evidently requires N^2 complex multiplications, plus a smaller number of operations to generate the required powers of W. Evaluating these sums directly would take $\mathcal{O}(N^2)$ arithmetical operations [7]. The FFT computes the same result in only $\mathcal{O}\Big(N\,\log(N)\Big)$ operations. In general, such algorithms depend upon the factorization of N, but (contrary to popular misconception) there are $\mathcal{O}\Big(N\,\log(N)\Big)$ FFTs for all N, even prime n. The difference between $N\,\log(N)$ and N is immense: With $N = 10^6$, for example, it is the difference between, roughly, 30 seconds of CPU time and two weeks on a microsecond cycle time computer [39]. Since the inverse DFT is the same as the DFT, but with the opposite sign in the exponent and a $1/N$ factor, any FFT algorithm can easily be adapted for it as well. By far the most common FFT is the Cooley-Tukey algorithm. This method (and the general idea of an FFT) was popularized by a publication of J. W. Cooley and J. W. Tukey in 1965 [10], but it was later discovered that those two authors had independently re-invented an algorithm known to Carl Friedrich Gauss around 1805 [16] (and subsequently rediscovered by as many as a dozen individuals in limited forms [18]). This is a divide and conquer algorithm that recursively breaks down a DFT of any composite size $N = N_1\,N_2$ into many smaller DFTs of sizes N_1 and N_2, along with $\mathcal{O}(N)$ multiplications by complex roots of unity traditionally called twiddle factors. Also, because the Cooley-Tukey algorithm breaks the DFT into smaller DFTs, it can be combined arbitrarily with any other algorithm for the DFT. Finally, although the basic idea is recursive, most traditional implementations rearrange the algorithm to avoid explicit recursion.

One rediscovery of the FFT, that of Danielson and Lanczos in 1942 [11], provides one of the clearest derivations of this algorithm. The Danielson and Lanczos lemma shows that a discrete Fourier transform of length N can be rewritten as the sum of two discrete Fourier transforms, each of length $N/2$. One of the two is formed from the even-numbered points of the original N, the other from the odd-numbered points. The proof is simply this:

$$\begin{aligned} F_n &= \sum_{j=0}^{N-1} \mathrm{e}^{-2\pi i \frac{j\,n}{N}}\, f_j \\ &= \sum_{j=0}^{N/2-1} \mathrm{e}^{-2\pi i \frac{n}{N}(2j)}\, f_{2j} + \sum_{j=0}^{N/2-1} \mathrm{e}^{-2\pi i \frac{n}{N}(2j+1)}\, f_{2j+1} \\ &= \sum_{j=0}^{N/2-1} \mathrm{e}^{-2\pi i \frac{j\,n}{N/2}}\, f_{2j} + W^n \sum_{j=0}^{N/2-1} \mathrm{e}^{-2\pi i \frac{j\,n}{N/2}}\, f_{2j+1} \\ &= F_n^e + W^n\, F_n^o \ . \end{aligned} \tag{93}$$

In the last line, W is the complex constant, F_n^e denotes the n^{th} component of the Fourier transform of length $N/2$ formed from the even components of the original f_j's, while F_n^o is the corresponding transform of length $N/2$ formed from the odd components. It is worthwhile to note that the evaluation of the DFT by just one splitting of the input sequence requires $N^2/2$ multiplications and $N^2/2$ additions which is a factor-of-two-savings, that is encouraging for further splitting. Although there are ways of treating other cases, by far the easiest case is the

one in which the original N is an integer power of 2. With this restriction on N, it is evident that we can continue applying the Danielson-Lanczos lemma until we have subdivided the data all the way down to transforms of length one. The Fourier transform of length one is just the identity operation that copies its one input number into its one output slot $\Big(\mathcal{F}\{A\,\delta(t)\} = A,$ with $A =$ constant $\Big)$!

This algorithm which belongs to the class of the *decimation-in-time* since it involves the splitting of the input (or time) sequence consists of two phases: a reordering stage in which the input array is successively subdivided into even and odd sequences and a combine phase, in which sequences of length 1 are combined into sequences of length 2 then sequences of length 2 into sequences of length 4 and so on until the final transform sequence is formed from two sequences of length $N/2$. The following table 4.3 explains how to perform the former phase in a smart way, by means of the so-called bit-reversing order [39, 7]. Suppose

1	000	001	010	011	100	101	110	111
2	0	1	2	3	4	5	6	7
3	0				1			
4	0	2	4	6	1	3	5	7
5	00		01		10		11	
6	0	4	2	6	1	5	3	6
7	000	001	010	011	100	101	110	111
8	0	4	2	6	1	5	3	7

FIGURE 4.3. Reordering phase in the case of 8 samples.

that the input array consists, for simplicity of 8 samples, numbered from 0 to 7 (line 2). Moving the evens on the left side of table and the odds on the right means in other words to separate those positions which have rest 0 from those which have rest 1 when divided by 2, as indicated in the third line, yielding two sequences by four elements each. Inside these two new sequences (line 4) it is still possible to distinguish even and odd positions, which are rearranged as showed in line 6. This step corresponds to a further division by 2 whose rest is indicated as the second digit in line 5. Keeping on splitting the input sequence in an even/odd fashion until N sequences of length 1 remain, and assigning successively a 0 to the even and a 1 to the odd sequences, is evidently nothing else than the standard technique to convert from decimal to binary notation. Observing the first and the penultimate line of the table, it is evident that the original array is now rearranged in a fashion which could be directly obtained by simply reversing the binary sequences of its original entries, i.e. position number 4_{10}, $(100)_2$, goes finally to position 1, because $1_{10} = (001)_2$.

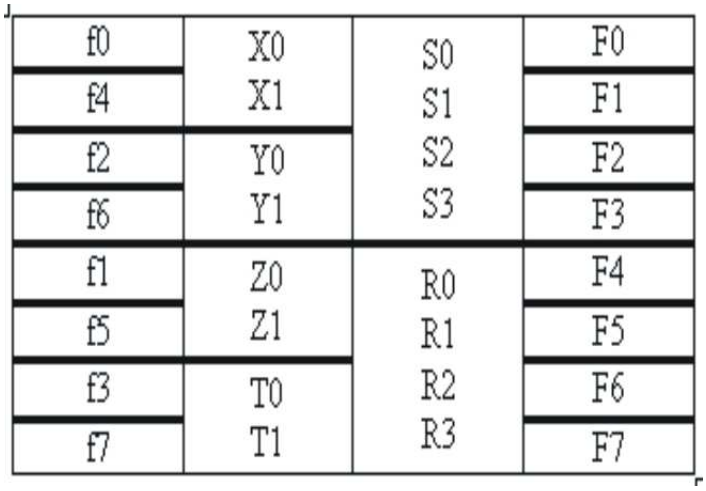

FIGURE 4.4. Combine phase in the case of 8 samples.

The combine phase starts now with N trivial one-point transforms. Then the sequences of length 1 are combined in pairs (f_0 with f_4, f_2 with f_6 ...) according to formula (93) to form DFTs of length 2 (see table 4.4). Again, DFTs sequences of length 2 are combined in pairs (X_0 and X_1 with Y_0 and Y_1 ...) to form two DFTs of length 4 ($N/2$) and finally these two are combined to form the desired F_k (see table 4.4).
Each combination takes of order N operations, and there are evidently $\log_2(N)$ combinations, so the whole algorithm is of order $N \log_2(N)$ (assuming, as is the case, that the process of sorting into bit-reversed order is no greater in order than $N \log_2(N)$). This, then, is the structure of an FFT algorithm: It has two sections. The first section sorts the data into bit-reversed order, but this takes no additional storage, since it involves only swapping pairs of elements (If k_1 is the bit reverse k_2, then k_2 is the bit reverse of k_1). The second section has an outer loop that is executed $\log_2 N$ times and calculates, in turn, transforms of length 2, 4, 8, .., N. For each stage of this process, two nested inner loops range over the subtransforms already computed and the elements of each transform, implementing the Danielson-Lanczos lemma. The operation is made more efficient by restricting external calls for trigonometric sines and cosines to the outer loop, where they are made only $\log_2(N)$ times. Computation of the sines and cosines of multiple angles is through simple recurrence relations in the inner loops.

Problems and Remedies. The most important class of signals appearing in practical applications are those with an arbitrary unlimited shape in **c**-space which are not band limited in **k**-space. To obtain a discrete signal one has to multiply the arbitrary distribution function $f_{scat}(c)$ with the sampling (or repetition) function $\mathrm{rep}_{C_s}\delta(c) = \sum_{n=-\infty}^{\infty} \delta(c - n\,C_s)$ $\Big($with the transform pair: $\mathrm{rep}_{C_s}\delta(c) \Leftrightarrow \frac{1}{C_s}\mathrm{rep}_{1/C_s}\delta(k)$ $\Big)$ to get

$$f_s(c) = f_{scat}(c)\ \mathrm{rep}_{C_s}\delta(c) = \sum_{n=-\infty}^{\infty} f_{scat}(nC_s)\ \delta(c - n\,C_s)\ , \tag{94}$$

where C_s is the sample interval. In general, the spectrum $\hat{f}_{scat}(k)$ of the signal $f_{scat}(c)$ is not band limited and aliasing is natural consequence of the sampling process. To reduce the influence of aliasing it is recommended to sample the signal with high "frequency" $1/C_s$ which means, with a sufficient small C_s.
Clearly, the discrete signal (94) is not suitable for numerical purposes because an infinite number of sampling points are used. Therefore, the sampling signal $f_s(c)$ have to be limited in velocity space by the application, for instance, of the rectangle function of unit height

$$\mathrm{rect}_{C_0}(c) = \begin{cases} 1\ , & \frac{C_s}{2} \le c \le C_0 - \frac{C_s}{2} \\ 0\ , & \text{else} \end{cases} \ , \tag{95}$$

where C_0 is the duration of the limitation and $\mathrm{rect}_{C_0}(c) \Leftrightarrow \mathrm{e}^{-\pi i k (C_0 - C_s)}\ \frac{sin(\pi k C_0)}{\pi k}$. Then, the velocity limitation yields

$$f_w(c) = f_s(c)\ \mathrm{rect}_{C_0}(c) = \sum_{n=0}^{N-1} f_{scat}(nC_s)\ \delta\big(c - n\,C_s\big)\ , \tag{96}$$

where it is assumed that N equidistant δ-functions occur within the period of observation, that is $C_0 = N\,C_s$. The difficult point concerns the choice of the duration of the observation. It is well-known that for the ideal case of a band limited periodic signal the observation duration C_0 should be the period of the signal or a multiple of this period. Otherwise – greater than a period –, additional "frequency" components are generated in the Fourier transform $\hat{f}_{scat}(k)$, which leads to ripples in the spectrum and sharp discontinuities of the signal in velocity space. These discontinuities are also expected in the case of an arbitrary signal, where the period is determined by the number N of sampling points. A convenient remedy to cure these "errors" (side lobes amplitudes) is to replace the rectangle velocity limitation by a more appropriate window functions. The net effect, for instance, of the Hanning-function is a strong attenuation of the rectangle function induced discontinuities [39, 7].

Interpolation Block. After the grid-based computations are executed, the essential information (derivation of the Rosenbluth potentials) has to be brought onto the particle location in velocity space. This link between the grid-based and mesh-free numerical model is established by the interpolation step, which is nothing else than the inverse operation of the assignment procedure. The friction and diffusion coefficients $R_p(t_n) = \Big\{F_\rho,\ D_{\rho\sigma};\ \alpha, \beta = 1, 2, 3\Big\}$ at the velocity $\vec{V}_p^{\,n}$ of the p^{th} particle at time t_n are computed from the coefficients $R^n_{i,j,k}$ stored at the surrounding nodes $\vec{v}_{i,j,k}$ of the actual velocity grid. For this task, we apply the volume-weighting interpolation formula [19]

$$R_p(t_n) = \sum_{\mu,\nu\lambda=0}^{1} g^{(p)}_{i+\mu,j+\nu,k+\lambda}\ R^n_{i+\mu,j+\nu,k+\lambda}\ , \tag{97}$$

where the weights $g^{(p)}_{i,j,k}$ are already determined in the assignment step. The fact that the particle-based weights (97) have to be computed only once at the interface mesh-free/grid-based and used for assignment as well as for interpolation is a very attractive feature, which

enhance the efficiency of the numerical scheme. Finally note, that the way of computing the particle weights (86) reveals that interpolation and assignment are multidimensional linear approximations.

Langevin Solver. Simulations of phenomena caused by a non-neutral plasma requires the solution of the time-dependent Maxwell-Vlasov equations in two or even three dimensions in space [32]. The numerical method of choice to solve this non-linear problem is the PIC method. There, the Lorentz force at the charged particle position is responsible for the redistribution of the different particle ensembles. The new phase-space coordinates are obtained by the numerical solution of the deterministic Lorentz equations, where the special tailored leapfrog scheme of Boris is applied [5]. In the context of the present PIC approach, the Langevin "forces", which consists of the deterministic friction and the stochastic diffusion moves the particles in velocity space. Under the action of this velocity-dependent Langevin forces, each particle evolve in velocity space according to the Langevin-type equation (52). However, this equation represents a SDE whose mathematical character contrasts sharply with the deterministic Lorentz equation. Especially, this fundamental difference find expression in the numerical approximation of the stochastic law of dynamics (52). Within the here considered Fokker-Planck module, we are interested in the individual trajectories of the dynamical system described by this SDE. To obtain a pathwise good approximation of equation (52) in our direct simulations, we apply explicit strong Itô-Taylor schemes. As discussed in detail previously (see Section 3.6), we used the scheme

$$\begin{aligned} \vec{C}^{\,n+1} &= \vec{C}^{\,n} + \Delta t_n \, \vec{F}\Big(\vec{C}^{\,n}, t_n\Big) + \sqrt{\Delta t_n} \sum_{q=1}^{3} \vec{b}_q^{\,n} \, \eta_{n+1}^q \quad \text{(Euler)} \\ &+ \sum_{p,q=1}^{m} \vec{b}_p^{\,n} \cdot \nabla_c \, \vec{b}_q^{\,n} \, \mathrm{I}_{(p,q)} \qquad\qquad \text{(Milstein)} \end{aligned} \tag{98}$$

which converges strongly with order up to $\gamma = 1$, where $\eta_{n+1}^q \sim \mathcal{N}(0,1)$ and the derivatives and $\mathrm{I}_{(p,q)}$ are approximated by (74) and (76), respectively.

5. Results

The goal of this section is the assessment of the Fokker-Planck module which is used for the self-consistent computation of the friction and diffusion coefficients arising from the diffusive treatment of intra-species collision. For that, we first present a sequence of numerical experiments in one-dimensional velocity space in order to study the quality, property and reliability of the approximation characteristics of each building block of the FP module seperately. Afterwards, a further numerical test problem should demonstrate the approximation properties of the complete code. Finally, in order to gain additional experience with the applied numerical methods, we consider the collisional relaxation of an isotropic non-Maxwellian to the equilibrium particle distribution function.

5.1. **Experiment 1: Mesh-free / Grid-based Interface Handling.** Since interpolation is the inverse operation of the assignment procedure, we restrict ourselves to inspect the latter one in this experiment. For this, we generate $N = 10^4$ Gaussian distributed (pseudo) random numbers with mean $\mu = 3$ and variance $\sigma^2 = 4$ according to the Müller-Box method [39] and the transformation

$$X_i = \sigma\, G_i + \mu\ ; \quad i = 1, \ldots, N\ , \tag{99}$$

where $G_i \sim \mathcal{N}(0,1)$, which represent the velocity of the N particles in mesh-free velocity space. After the localization with respect to the velocity grid, each particle contributes according to its weights (86) to the particle distribution function, which is depicted in Figure 5.1 for a coarse ($N_G = 32$) and a fine ($N_G = 64$) velocity grid. As we would expect, the Gaussian recorded on the coarse velocity mesh (line with open circles) is slightly broadened compared to the analytical result (full line), which results in the reduced maximum height. Clearly, the doubling of the discretization points ($N_G = 64$) cures this inaccuracy as seen in the lower plot of Figure 5.1. From this numerical experiment we conclude that the linear approximation established by the assignment and interpolation procedures in conjunction with a moderate fine discretization of the velocity grid is sufficient for our purposes.

5.2. **Experiment 2: Grid-based Approximations (Rosenbluth Solver).** The central task of this building block is to provide the grid-based Rosenbluth potentials and their derivatives. For this, we apply DFTs which are most effectively algorithmical realized by FFT techniques. To demonstrate the quality and property of the coded Cooley & Turkey algorithm, we simulate the approximation path outlined in sub-section 2.2.1 inclusive the back transformation to velocity space. For that, we prescribe the Gaussian

$$f(w) = \frac{2}{\sqrt{2\pi}\, v_{\mathrm{th}}^3} \exp\left(-\frac{w^2}{2v_{\mathrm{th}}^2}\right) \tag{100}$$

with the temperature $T_e^\star = 10$ eV on the velocity grid. Afterwards, we compute the convolutions (8) - (11) in **k**-space and perform the inverse DFT to velocity space. The results of this proceeding (open squares) and the analytical solution (full line) is seen in Figures 5.2 till 5.4, where the velocity space is discretized by $N_G = 32$ grid points. Obviously, this comparison indicates that the Rosenbluth solver produces accurate approximations and runs in a very

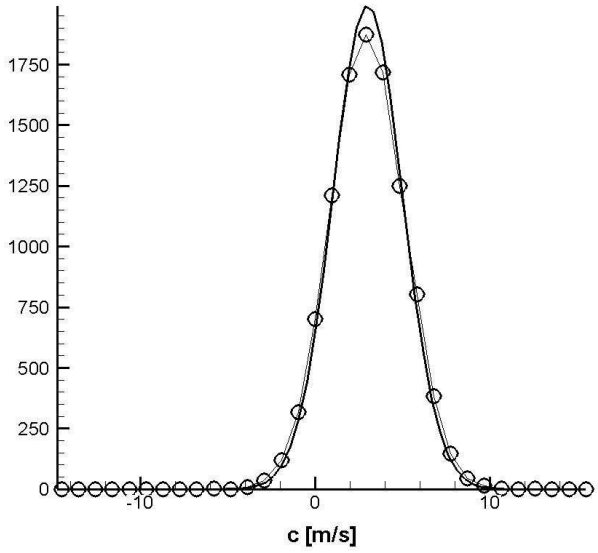

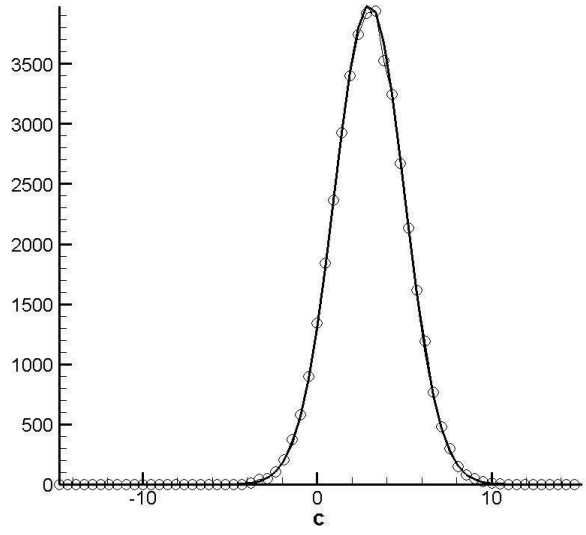

FIGURE 5.1. Reconstruction of the velocity distribution function from $N = 10^4$ particles with Gaussian distributed random velocities ($\mu = 3$, $\sigma = 2$). The discretization of the velocity grid is established by $N_G = 32$ (upper) and $N_G = 64$ (lower plot) nodes.

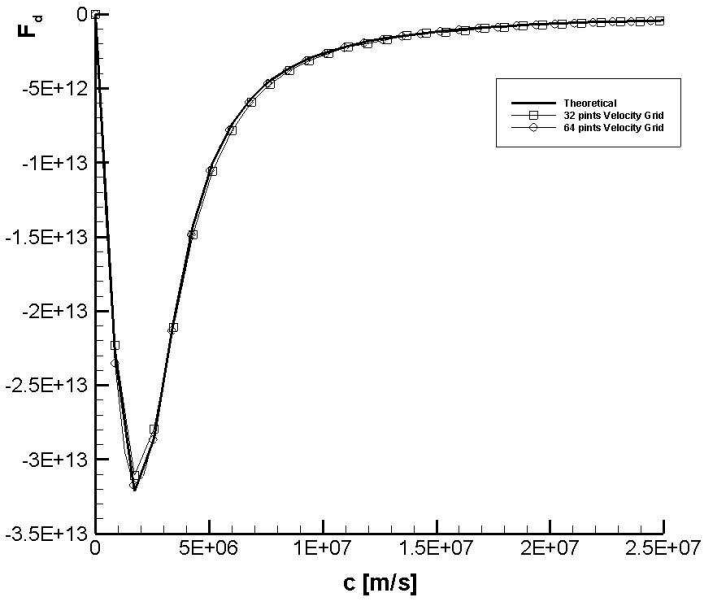

FIGURE 5.2. Fiction coefficient as a function of velocity obtain with the Fourier approach (squares: $N_G = 32$ and circles: $N_G = 64$ grid points) and the analytical solution (full line).

reliable manner. In order to investigate the influence of the velocity-grid discretization to the approximation behavior, we rerun the computations for a finer ($N_G = 64$; open circles) mesh. For comparison, these results are also plotted in the Figures 5.2 - 5.4. Clearly, we observe the tendency of the finer grid to better resolve, especially, the high-energy tail, which is explicitly seen in Figure 5.3, where the second derivative of the Rosenbluth potential $\mathcal{G}$ is approximated. The results obtained with the Rosenbluth solver recommend this building block for the application of self-consistent friction and diffusion coefficients computing arising from Fokker-Planck treatment of collisions.

5.3. **Experiment 3: Mesh-free Approximations (Langevin Solver).** The particles law of motion in mesh-free velocity space is established by the SDE (39), where the friction and diffusion coefficients are unknown functions of velocity and time. The intention of the present experiment is to study the approximation behavior and quality of the applied explicit Itô-Taylor schemes (98), which are one building block of the Fokker-Planck module. To do this, we start from the very simple – but analytical solvable – situation, where the friction and diffusion are given by

$$F(V,t) = -\,a\,V(t) \quad \text{and} \quad D(V,t) = \sigma^2\ , \tag{101}$$

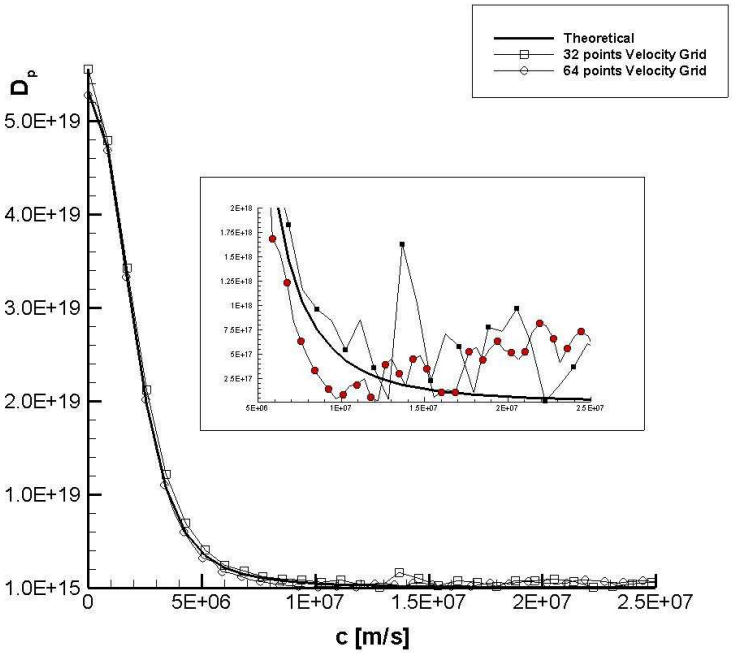

FIGURE 5.3. Velocity-dependent parallel diffusion coefficient computed with the discrete Fourier approach (squares: $N_G = 32$ and circles: $N_G = 64$ grid points) and the analytical solution (full line).

respectively, with constants a and σ. The corresponding linear SDE (which is the Langevin equation) reads as

$$dV(t) = -a\,V(t)\,dt + \sigma\,dW(t) \tag{102}$$

and possesses the analytical solution [23]

$$V(t) = \mathrm{e}^{-a\,(t-t_0)}\,V_0 + \sigma\,\mathrm{e}^{-a\,t}\int_{t_0}^{t} dW_s\,\mathrm{e}^{a\,s}\;, \tag{103}$$

where V_0 denotes the initial value at $t = t_0$. Note, that the additive noise random forcing (102) is also known as (one-dimensional) Ornstein-Uhlenbeck process [15, 23]. If we interpret the appearing Itô integral in (103) as a random number, then $V(t)$ represents a time-dependent random number whose mean and variance are found to be [23]

$$m_v(t) = \mathrm{e}^{-a\,(t-t_0)}\,V_0 \tag{104}$$

and

$$s_v^2(t) = \frac{\sigma^2}{2\,a}\Big(1 - \mathrm{e}^{-2\,a\,(t-t_0)}\Big)\;, \tag{105}$$

respectively. Furthermore, we note that the FP equation for the transition probability $p(V,t)$ corresponding to (102) (see Section 3.4) also has a closed solution of the form (see Appendix

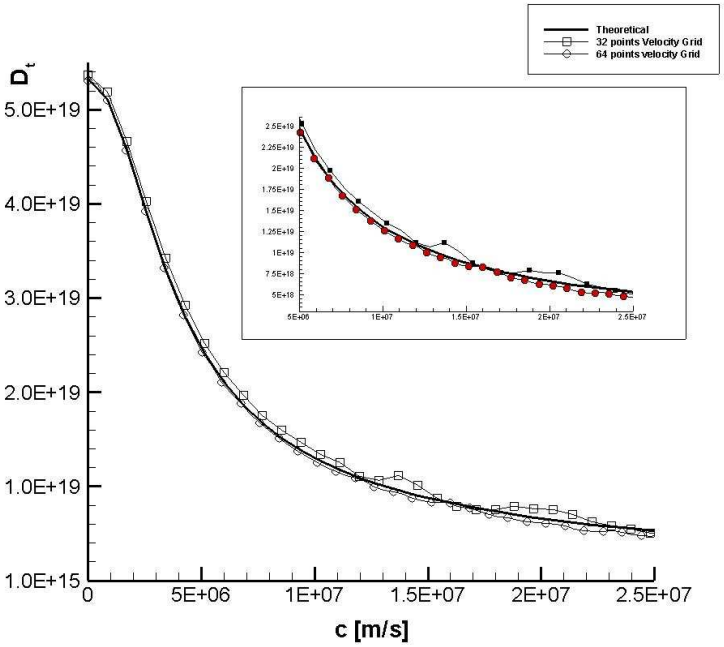

FIGURE 5.4. Transversal diffusion coefficient as a function of velocity computed with the discrete Fourier approach (squares: $N_G = 32$ and circles: $N_G = 64$ grid points) and the analytical solution (full line).

G)

$$p(V,t) = \frac{1}{\sqrt{2\,\pi} s_v}\, \mathrm{e}^{-\frac{(V-m_v)^2}{2\,s_v^2}}\,, \tag{106}$$

where m_v and s_v are given by (104) and (105). Clearly, for large times $t >> t_0$ the mean value m_v vanishes and the variance tends to $s_v^2 \to \frac{\sigma^2}{2\,a}$, which means that both $p(V, t \to \infty)$ and the corresponding probability density function arrive their equilibrium states.

The short discussion suggests to design the numerical experiment in such a way that the mean and variance as well as particle distribution (on the velocity grid) are "measureable" quantities which could be compared with their analytical counterparts. For that, we use $N = 4 \cdot 10^4$ test particles, where each of them has the same initial velocity $V_0 = 2$ (we drop the units in this experiment, for convenience) in the mesh-free velocity space. Afterward, all particles are forced according to the Langevin equation (102) – which is solved by the schemes (98) for $\Delta t = 2.5 \cdot 10^{-4}$ –, where the constants are fixed equal to $a = 0.5$ and $\sigma = 2$. The observables of the numerical experiment in mesh-free space are the mean and variance which are determined according to

$$\tilde{m}_v(t) = \frac{1}{N} \sum_{p=1}^{N} V_p(t) \tag{107}$$

and

$$\tilde{s}_v^2(t) = \frac{1}{N-1}\sum_{p=1}^{N}\Big[V_p(t) - \tilde{m}_v(t)\Big]^2 , \tag{108}$$

respectively, where $V_p(t)$ denotes the actual velocity of the particles. These quantities as well as their analytical counterparts (104) and (105) are recorded each 500 temporal cycles. The results for the mean value and the variance are depicted in Figures 5.5 and 5.6, respectively, where the Euler approximation (line with filled squares) and the exact solution (full line) is plotted. Obviously, the overall agreement of the numerical result with the analytical

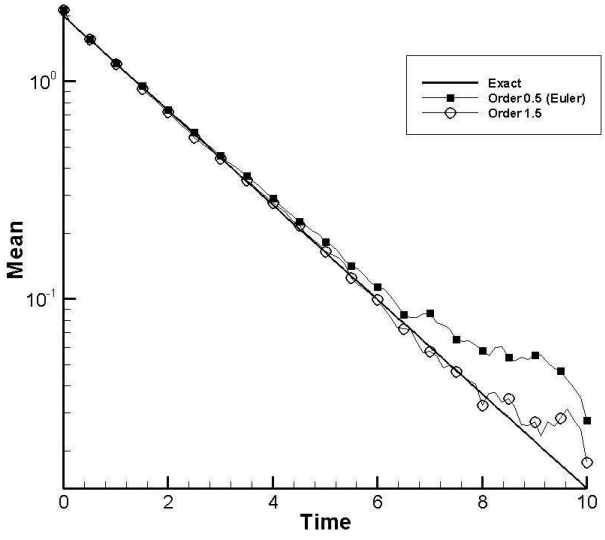

FIGURE 5.5. Temporal evolution of the mean value of the Ornstein-Uhlenbeck process. Full line: exact solution, line with filled squares: Euler approximation ($\gamma = 0.5$), line with open circles: $\gamma = 1.5$ strong order Itô-Taylor scheme

solution is very satifactory. The deviations between the Euler approach and the exact result seen for the mean value in Figure 5.5 can be "cured" by using, for instance, a $\gamma = 1.5$ strong order Itô-Taylor scheme [24] (line with open circles). Note, that $\gamma = 1.5$ is the next 'valid' order of approximation because the coefficient function $B(V,t)$ is constant for the Ornstein-Uhlenbeck process (see scheme (69)). An overview of the temporal evolution of the particle distribultion function on the velocity grid is seen in Figure 5.7, where the Euler approximation is used to solve the Langevin equation (102). These snapshots clearly demonstrate that the particle distribution of the Ornstein-Uhlenbeck process tends to the expected Gaussian shape distribution. We emphasize that this equilibrium state is reached approximately at $t = 5$ (see also Figure 5.6); afterward, the change of the shape is hardly visible in this representation.

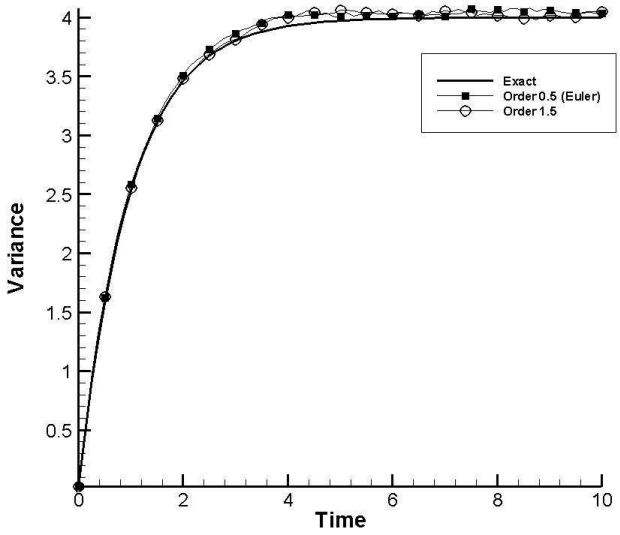

FIGURE 5.6. Comparison between the time-dependent variance obtained with a strong Euler ($\gamma = 0.5$, line with filled squares) and a strong Itô-Taylor ($\gamma = 1.5$, line with open circles) scheme and the analytical result (full line).

A further comparison between the numerical results of the Euler scheme (open circles) and the exact solution (full line) is seen in Figure 5.8, where the particle distribution function on the velocity grid is plotted at time $t = 10$. This as well as the other results presented in this section convince us from the quality and reliability of the Langevin solver which is now used for self-consistent collision simulations.

REMARK: This numerical experiment is tailored to study the moments of the particle velocities which are represented by random numbers (103). This means, that we are not interested in pathwise good approximation of the SDE (102). In fact, we used the strong Itô-Taylor schemes based on Gaussian distributed random numbers for the so-called weak approximation of the Langevin equation (102) [24]. In this case, we have much more freedom in generating the "noise increments", that is, we can use here two- or three-point distributed random variables instead Gaussian random numbers. Furthermore, note that the (weak) approximation order in the considered case is $\beta = 1$ and $\beta = 2$ for the applied Euler and Itô-Taylor schemes, respectively.

5.4. **Experiment 4: Interplay of the different Building Blocks (Fokker-Planck Module).** This numerical experiment is designed for the assessment of the applied numerical methods coded in the FP module. Moreover, diagnostic tools are introduced to get a better

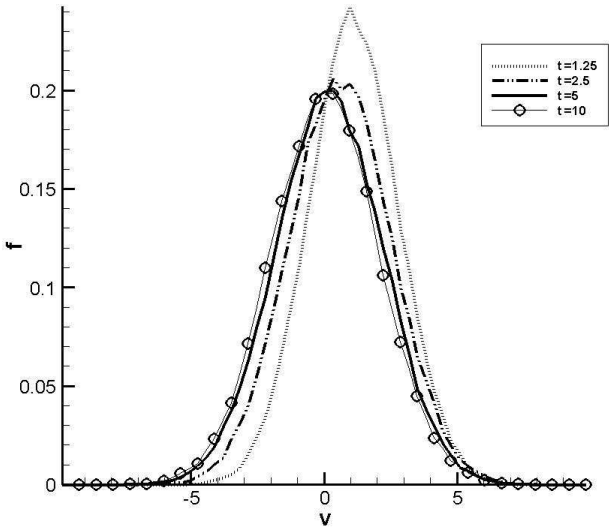

FIGURE 5.7. Collisional relaxation of the Ornstein-Uhlenbeck distribution function to the equilibrium. The distribution function is recorded on the velocity grid at $t = 1.25$ (dotted), $t = 2.5$ (dashed-dotted), $t = 5$ (full line) and $t = 10$ (line with open circles).

characterization of the relaxation process, which could help to identify possible insufficiencies as well as to suggest further improvements.

The starting point of the current experiment is the fact that the isotropic function $h(c) = c^2 f(c)$ with the Gaussian distribution $f(c)$ (see relation 100) represents a solution of the FP equation (38) [29]. According to the results of Section 3.4, the corresponding Langevin-type SDE has the form

$$dV(t) = \left[F(V) + \frac{D_\perp(V)}{V}\right] dt + \sqrt{D_\parallel(V)}\, dW(t) \,, \tag{109}$$

where the friction and diffusion coefficients for the isotropic case are given by (16) - (18) and plotted in Figure 2.2. Clearly, for isotropic considerations the latter equation (109) is coded in the Langevin solver.

The numerical experiment is initialized as follows: In the mesh-free velocity space, the initial velocities V_p^0 of the $N = 2 \cdot 10^5$ particles are determined from

$$V_p^0 = \sqrt{V_{p,1}^2 + V_{p,2}^2 + V_{p,3}^2} \,, \tag{110}$$

where the $V_{p,i} \sim \mathcal{N}(0, \sigma^2)$ are independent identically distributed Gaussian random numbers (with mean zero and variance $\sigma^2 = v_{\text{th}}^2$). This procedure ensures that the initial velocity distribution of the particles – which is the probability density function of the random numbers

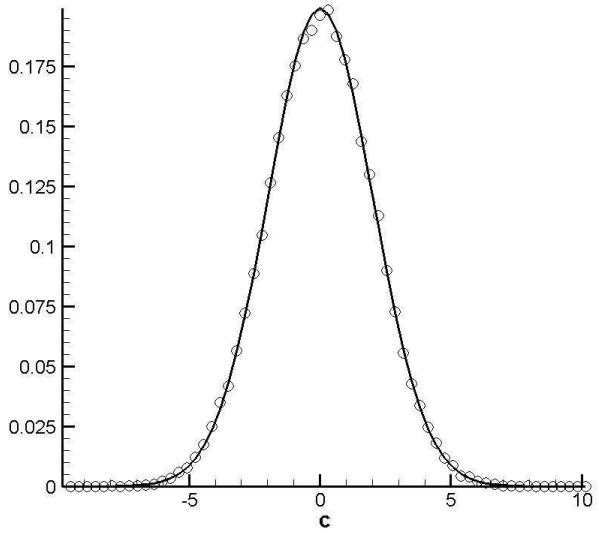

FIGURE 5.8. Comparison between the numerical (Euler scheme; open circles) and analytical (full line) particle distribution function recorded on the velocity grid at $t = 10$.

V_p^0 – is a Maxwellian [20] of the form

$$h(c,0) = g_0(c) = \frac{2}{\sqrt{2\pi}} \frac{c^2}{v_{\mathrm{th}}^3} \exp\left(-\frac{c^2}{2v_{\mathrm{th}}^2}\right), \tag{111}$$

where the thermal velocity $v_{\mathrm{th}}^2 = k_B\, T_e / m_e$ is adjusted for a temperature $T_e^\star = 10$ eV. Subsequently, the PIC cycle seen in Figure 4.1 is $2 \cdot 10^4$ times passed through, which is equivalent to a simulation time of approximately 354.5 ns. Throughout this computation the velocity grid which is needed for the Rosenbluth solver consists of $2^6 = 64$ grid points. A first result is depicted in Figure 5.9: There, the theoretical (Maxwellian) curve (full line) together with the numerical solution (open circles) is plotted after $2 \cdot 10^4$ iterations. As we expected, the temporal evolution of the distribution function obtained from the simulation stays very close to the Maxwellian shape. Moreover, this result demonstrates that also the high-energy tail is reproduced very well, although the resolution of this part is often critical owing to the low number of particles. Furthermore, the friction (16) and transversal diffusion (18) coefficients obtained from the simulation (open circles) after $2 \cdot 10^4$ iterations and the analytical result for a Maxwellian (full line) are seen in the Figures 5.10 and 5.11, respectively. Obviously, these results once again document the high approximation quality and reliability of the Fokker-Planck solver. A basic concept for the characterization of an arbitrary (that means a non-equilibrium) velocity distribution function is the method of moments. Here, the

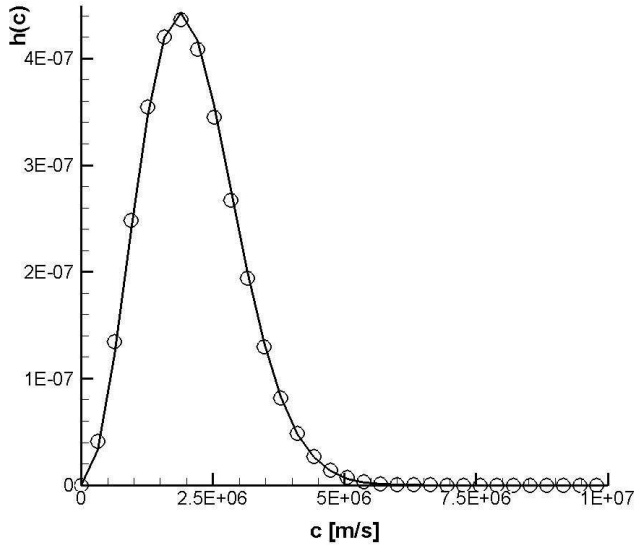

FIGURE 5.9. Numerical (open circles) and exact (full line)velocity distribution after $2 \cdot 10^4$ temporal iterations.

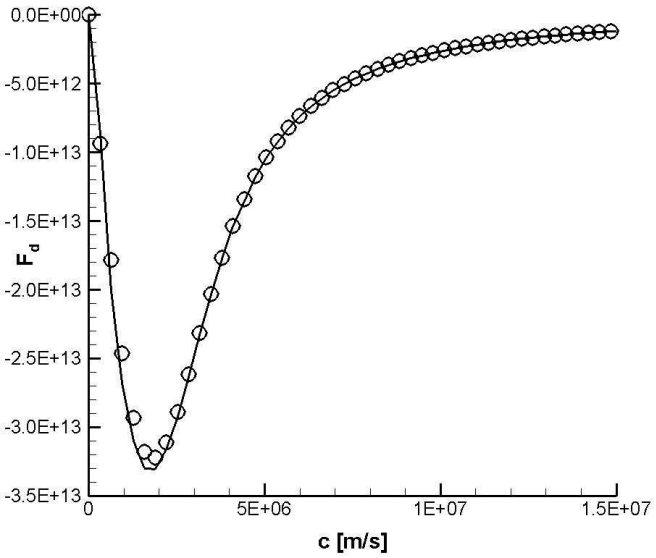

FIGURE 5.10. Friction coefficient from the analytical result for a Maxwellian (full line) and from the simulation (open circles) after $2 \cdot 10^4$ iterations.

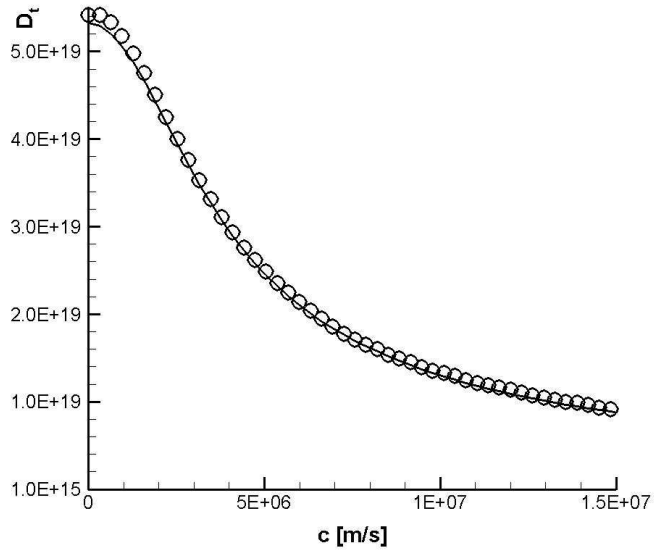

FIGURE 5.11. Comparison between the numerical (open circles) and the analytical (full line) result for the transversal diffusion coefficient after $2 \cdot 10^4$ iterations.

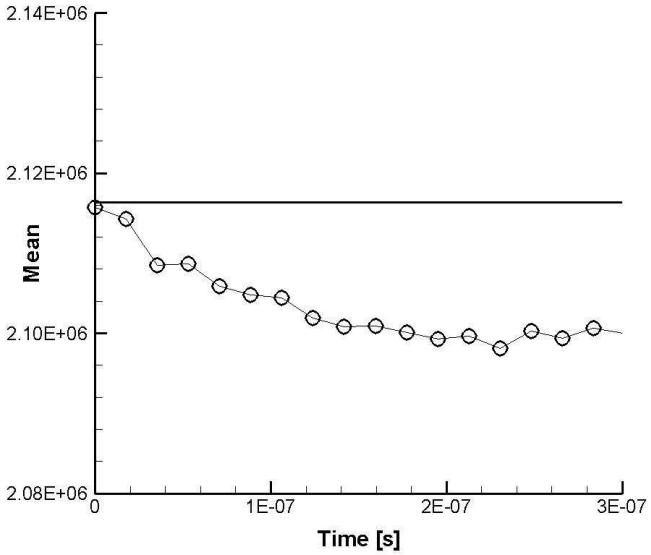

FIGURE 5.12. Temporal evolution of the of the numerical obtained (line with open circles) and exact (full line) mean value (first moment).

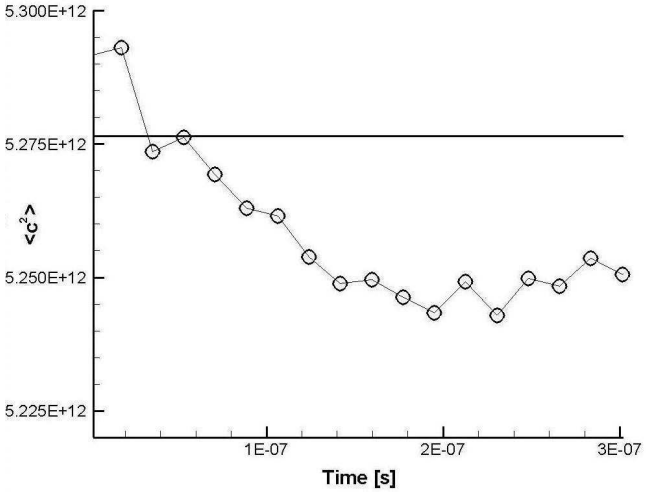

FIGURE 5.13. Temporal evolution of the computed (line with open circles) and exact (full line) second moment.

k^{th} moment of the distribution function $f_\alpha = f_\alpha(\mathbf{x}, \mathbf{c}, t)$ of specie "α" is defined by

$$< \mathbf{c}^k >_\alpha = \int_\Omega \mathbf{c}^k \, f_\alpha \, d^3c \quad ; \; k = 1, 2, \dots \quad , \tag{112}$$

where it is assumed that the velocity distribution is normalized: $\int_\Omega f_\alpha \, d^3c = 1$. The temporal evolution of the first two moments $< \mathbf{c} >_e$ and $< \mathbf{c}^2 >_e$ of the grid-based velocity distribution function $f_e = h(c, t)$ are seen in the Figures 5.12 and 5.13, respectively, together with their analytical counterparts. Obviously, the plots indicate that both numerical results (line with open circles) are below their exact values (full line) and slightly decrease in the course of the simulation. The observed deviations from the exact values may be attributed to the relatively "poor" approximation order of the Langevin solver ($\gamma = 1/2$) and the damping due to the linear assignment and interpolation procedures. The further helpful quantity in characterizing the distribution function is the variance

$$\mathsf{Var}_\alpha(\mathbf{c}) = \sigma_\alpha^2 = < \left(\mathbf{c} - < \mathbf{c} >_\alpha\right)^2 >_\alpha \, , \tag{113}$$

which estimates the mean squared-deviation of $\mathbf{c}$ from its mean value. The temporal evolution of this measure is monitored in Figure 5.14, where the numerical result (line with open circles) and the exact value (full line) are plotted. The slightly increasing shape of the curve above the exact value can be interpreted as natural consequence of assignment and interpolation which tend to broaden the distribution function resulting in an artificial heating of the particle ensemble. Another important figure of merit in analysis of systems in non-equilibrium is the local H-function [46, 12] applied in the form

$$H_\alpha(\mathbf{x}, t) = - \, < \ln(f_\alpha) >_\alpha \tag{114}$$

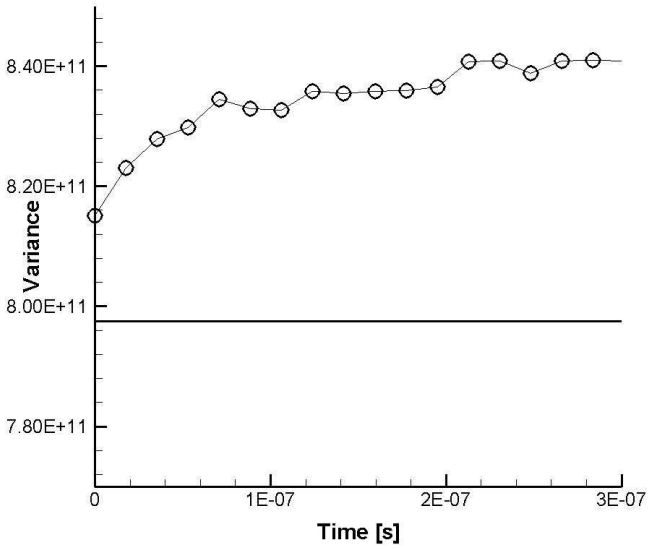

FIGURE 5.14. Temporal evolution of the of the numerical obtained (line with open circles) and exact (full line) variance σ_e^2.

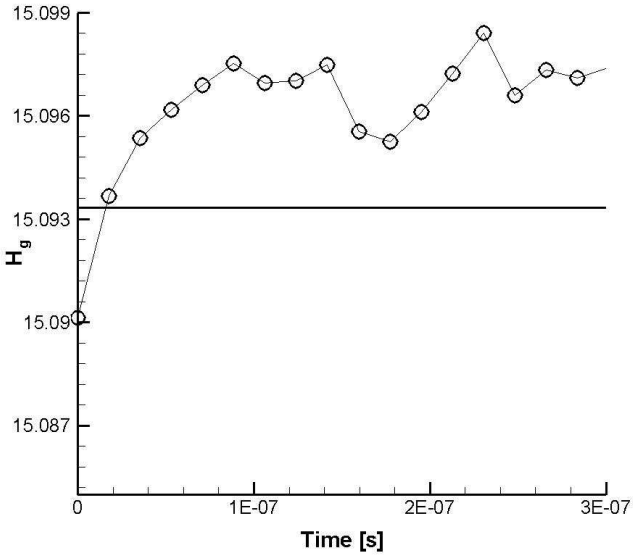

FIGURE 5.15. Temporal evolution of the of the computed (line with open circles) and exact (full line) H-function $H_e(t)$.

which can be ascribed to Boltzmann (1872). This quantity can be used to show that the entropy of a closed system can only increase in the course of time till it approaches a limit for very large times (H-theorem) [44, 12, 3]. In this respect, this quantity provides an appropriate measure of the extent to which the conditions of a system deviates from that corresponding to equilibrium. As shown in Figure 5.14, in this experiment the H-function stays approximately constant – besides small numerical oscillations – and slightly above the exact value, remarking the fact that the whole code can hold a steady-state solution quite well and confirming a very good synergy of the blocks previously considered.

5.5. **Arbitrary Isotropic Initial Distribution.** The final numerical experiment is tailored to study the collisional relaxation of an arbitrary isotropic initial velocity distribution to its equilibrium from first principles. The shape of the initial velocity distribution (see Figure 5.17 dashed-dotted line) is given by

$$h(c,0) = g_0(c) = \begin{cases} 3\,\frac{c^2}{\tilde{v}^3}, & \text{for } c \leq \tilde{v} \\ 0, & \text{for } c > \tilde{v} \end{cases}, \tag{115}$$

where $\tilde{v}$ is set equal to $\tilde{v} = \sqrt{5}\,v_{\text{th}}$ with a thermal velocity v_{th} corresponding to a temperature of $T_e^\star = 10$ eV. To establish such a velocity distribution, the initial velocities V_p^0 of the $N_p = 2 \cdot 10^5$ particles are chosen according to $V_p^0 = \tilde{v}\,U_p^{1/3}$, where the $U_p \in [0,\,1]$ are uniform random numbers between 0 and 1. The temporal evolution of the initial distribution (115) is monitored up to $2 \cdot 10^4$ cycles in time, where time step size is fixed equal to $\Delta t = 0.177$ ps and the discretization of the velocity grid is performed by 64 grid points. The first measurement of

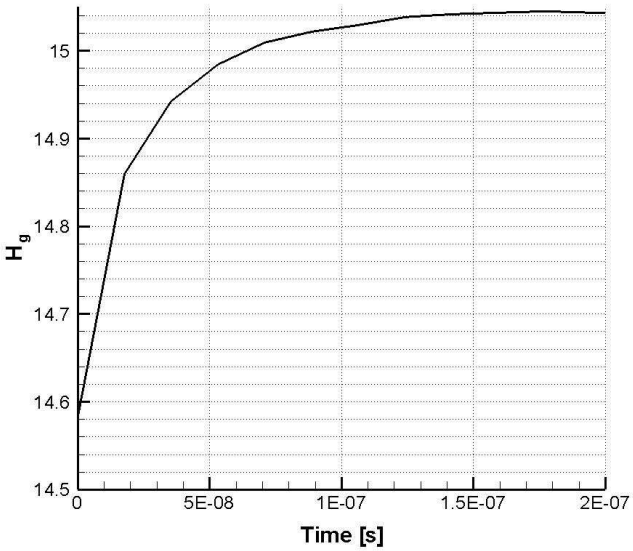

FIGURE 5.16. Temporal evolution of the H_e-function for the initial velocity distribution defined by relation (115).

interest is the temporal evolution of the $H_e(t)$-function (114), because the curve progression yields some information whether the equilibrium state of the system is reached or not. From Figure 5.16 we conclude that the equilibrium velocity distribution should be existent after approximately 150 ns ($\sim$ 8400 iterations). A further simulation result is depicted in Figure

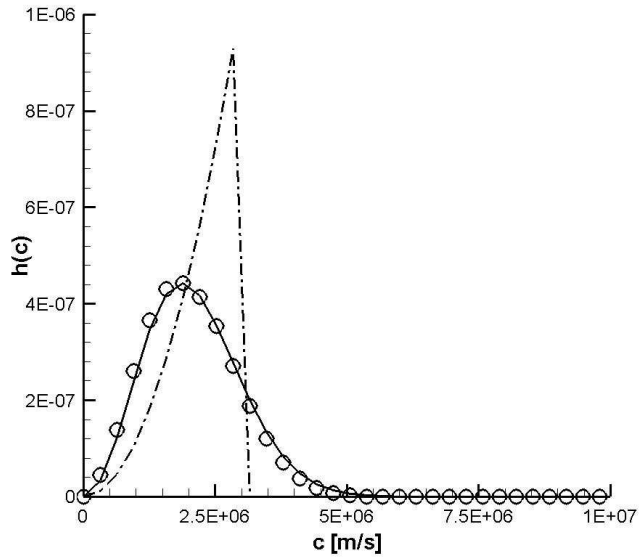

FIGURE 5.17. Temporal evolution of the initial velocity distribution (dashed-dotted line) to its equilibrium distribution function recorded after 10^4 iterations (open circles). For comparison a Maxwellian is plotted (full line) corresponding to a temperature of $T_e^\star = 10$ eV.

5.17, where the initial profile (dashed-dotted line) and the equilibrium velocity distribution (open circles) recorded after 10^4 temporal iterations are plotted. Additionally, the Maxwell velocity distribution corresponding to a temperature of $T_e^\star = 10$ eV is seen in Figure 5.17 as a full line. Clearly, this plot demonstrates that the final state of the collisional relaxation process agrees very well with the analytical Maxwellian shape for 10 eV. Note, that the numerical simulation slightly underestimate the high-energy tail of the velocity distribution. This observation is once again confirmed in Figure 5.18, where the function $f(c,t) = h(c,t)/c^2$ recorded after 2000 (dashed), 6000 (dashed-dotted line) and 14000 (line with circles) iterations is plotted with the analytical result (full line). Similar to previous investigations [27, 1], we observed for the proposed collision model that the high-energy part of distribution relax more slowly than the core of the velocity distribution function.

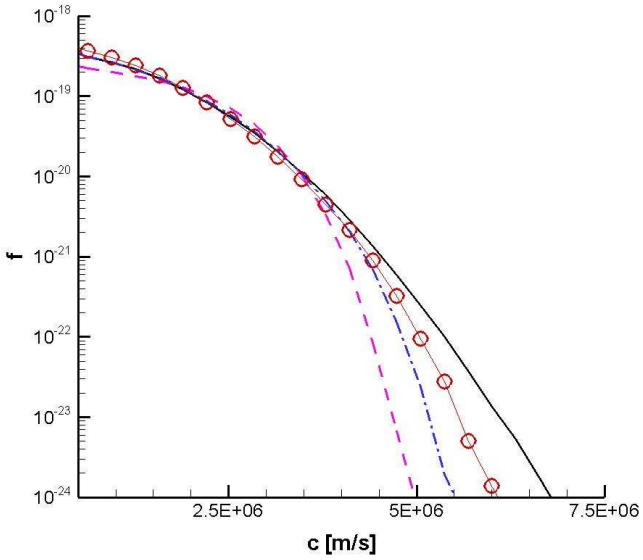

FIGURE 5.18. Comparison between the numerical simulation recorded at 2000 (dashed), 6000 (dashed-dotted) and 14000 (full line with circles) cycles and the analytical result (full line) for the velocity distribution function $f(c,t) = h(c,t)/c^2$.

6. Outlook

The most important near future goal is the extension of the existing Fokker-Planck module to a highly efficient, three-dimensional parallel production solver. For that, the reconstruction and interpolation strategies outlined in this report are already coded and tested. The three-dimensional FFT based on the algorithm of Cooley and Tukey is implemented, and an intensive testing campaign has been started to assess this building block. The low order Euler scheme for the numerical solution of the three-dimensional Langevin-type equation is available. However, higher order strong Itô-Taylor approximations seems to desireable in our opinion. Therefore, an explicit Milstein scheme has be constructed as proposed above, which is tested in a less optimized version. In order to parallelize the Fokker-Planck solver, we employ domain decomposition methods similar to those discussed in [41], where the parallelization tools MPI and OpenMP are used. However, this item in conjunction with parallelization endeavor of the complete hybrid code is still under investigation.

A further focal point will concern the question how to reduce statistical noise due to the finite number of particles in a spatial grid cell. This difficulty may be removed somewhat by averaging the particles distribution over several spatial cells to get a better statistical representation [41]. The possible drawbacks of such a proceeding are nonlocal (in space) momentum and energy exchange among the particles, which seemed to disagree with the physical situation on hand. An alternative to this approach consists in creating additional particles before sampling the distribution function on the velocity mesh and destroying these particles after the grid-based computations are finished [1, 47]. Another remedy for noise reduction may be obtained by the fact that the short-time behavior of the distribution function is characterized by a diffusion process. This means, the mean and variance have to be computed in an appropriate manner to estimate the local velocity distribution function. All the mentioned techniques should be assessed in near future to find out the suitable aspirant for the three-dimensional Fokker-Planck solver

A further focus of our scientific activities will include the construction and optimization of high-order approximations of the multi-dimensional Langevin-type equation. In this context additional investigations should decide whether both weak and strong approximations are suitable to model electron-electron scattering.

Acknowledgements

We gratefully acknowledge the Landesstiftung Baden-Württemberg for funding the present work.

References

[1] B. Albright, D. Winske, D. Lemons, W. Daughton, and M. Jones, *Quite simulation of Coulomb collision*, IEEE Trans. Plasma Sci., 31 (2003), pp. 19–24.

[2] M. Auweter-Kurtz, M. Fertig, D. Petkow, T. Stindl, M. Quandt, C.-D. Munz, P. Adamis, M. Resch, S. Roller, D. D'Andrea, and R. Schneider, *Development of a hybrid PIC/DSMC code*, (2005), pp. IEPC–2005–71; International Electric Propulsion Conference, Princeton, USA.

[3] G. Bird, *Molecular Gas Dynamics and the Direct Simulation of Gas Flows*, Clarendon Press, Oxford, 1994.

[4] C. Birdsall and A. Langdon, *Plasma Physics via Computer Simulation*, Adam Hilger, Bristol, Philadelphia, New York, 1991.

[5] J. P. Boris, *Relativistic plasma simulations – Optimization of a hybrid code*, in Proc. 4th Conf. on Num. Sim. of Plasmas, NRL Washington, Washington DC, 1970, pp. 3–67.

[6] W. Briggs and V. Henson, *The DFT*, SIAM, Philadelphia, 1995.

[7] E. Brigham, *The Fast Fourier Transform and its Application*, Prentice-Hall, Englewood Cliffs, 1988.

[8] R. Burton and P. Turchi, *Pulsed plasma thruster*, Journal of Propulsion and Power, 14 (1998), pp. 716–735.

[9] P. Clemmow and J. Dougherty, *Electrodynamics of Particles and Plasmas*, Addison Wesley, Reading, 1969.

[10] J. W. Cooley and J. W. Tukey, *An algorithm for the machine calculation of complex Fourier series*, Math. Comput., 19 (1965), pp. 297–301.

[11] G. Danielson and C. Lanczos, *Some improvements in practical Fourier analysis and their application to X-ray scattering from liquids*, J. Franklin Inst., 233 (1942), pp. 315–380, 435–452.

[12] S. DeGroot and P. Mazur, *Non-Equilibrium Thermodynamics*, Dover Publications, New York, 1984.

[13] D. Diver, *A Plasma Formulary for Physics, Technology, and Astrophysics*, Wiley-VCH Verlag, Berlin, 2001.

[14] M. Fedoruk, C.-D. Munz, P. Omnes, and R. Schneider, *A Maxwell-Lorentz solver for self-consistent particle-field simulations on unstructured grids*, Forschungszentrum Karlsruhe – Technik und Umwelt, **FZKA 6115**, (1998).

[15] C. Gardner, *Handbook of Stochastic Methods*, Springer Verlag, Berlin, Heidelberg, New York, 1985.

[16] C. F. Gauss, *"Nachlass: Theoria interpolationis methodo nova tractata", Werke, Band 3*, Königliche Gesellschaft der Wissenschaften, Göttingen, 1866.

[17] S. Hassani, *Mathematical Physics*, Springer, New York, Berlin, 1999.

[18] M. T. Heideman, D. H. Johnson, and C. S. Burrus, *Gauss and the history of FFT*, IEEE Acoustics, Speech, and Signal Processing Magazine, 1 (1984), pp. 14–21.

[19] R. Hockney and J. Eastwood, *Computer Simulation using Particles*, McGraw-Hill, New York, 1981.

[20] J. Honerkamp, *Stochastische Dynamische Systeme*, VCH Verlagsgesellschaft, Weinheim, 1990.

[21] G. Horwitz and E. Dagan, *The covariant Boltzmann-Fokker-Planck equation and its associated short-time transition probability*, J. Phys. A: Math. Gen., 21 (1988), pp. 1017–1028.

[22] R. Jahn, *Physics of Electric Propulsion*, McGraw-Hill, New York, 1968.

[23] P. Kloeden and E. Platen, *Numerical Solution of Stochastic Differential Equations*, Springer-Verlag, Berlin, Heidelberg, New York, 1992.

[24] P. Kloeden, E. Platen, and H. Schurz, *Numerical Solution of SDE Through Computer Experiments*, Springer-Verlag, Berlin, Heidelberg, New York, 2003.

[25] N. A. Krall and A. W. Trivelpiece, *Principles of Plasma Physics*, McGraw-Hill, New York, 1973.

[26] M. Laux, *Direkte Simulation verdünnter, reagierender Strömungen*, PhD thesis, Institut für Raumfahrtsysteme, Universität Stuttgart, Germany, 1996.

[27] W. Manheim, M. Lampe, and G. Joyce, *Langevin representation of Coulomb collision in PIC simulation*, Journal of Computational Physics, 138 (1997), pp. 563–584.

[28] M. Mitchner and C. Kruger, *Partially Ionized Gases*, Wiley, New York, 1973.

[29] D. Montgomery and D. Tidman, *Plasma Kinetic Theory*, McGraw-Hill, New York, 1964.

[30] R. Morse and C. Nielson, *Numerical simulation of the Weibel instability in one and two dimensions*, Physics of Fluids, 14 (1971), pp. 830–840.

[31] C.-D. Munz, P. Omnes, and R. Schneider, *A three-dimensional finite-volume solver for the Maxwell equations with divergence cleaning on unstructered meshes*, Computer Physics Communications 130 (2000) 83-117, (1999).

[32] C.-D. Munz, R. Schneider, E. Sonnendrücker, E. Stein, U. Voss, and T. Westermann, *A finite-volume particle-in-cell method for the numerical treatment of the Maxwell-Lorentz equations on boundary-fitted meshes*, Int. J. Numer. Meth. Engng., 44 (1999), pp. 461–487.

[33] C.-D. Munz, R. Schneider, and U. Voss, *A finite-volume particle-in-cell method for the numerical simulation of devices in pulsed power technology*, Surv. Math. Ind., 8 (1999), pp. 243–257.

[34] A. Nawaz, M. Auweter-Kurtz, G. Herdrich, and H. Kurtz, *Investigation and optimization of an instationary MPD thruster at IRS*. International Electric Propulsion Conference, Princeton, USA, October 31 - November 4, 2005.

[35] A. Nawaz, M. Auweter-Kurtz, H. Kurtz, and H. Wagner, *Pulsed plasma thrusters for primary propulsion and attitude control of a small all electrical satellite*. International Space Propulsion Conference, Sardinia, Italy, June 7-8, 2004.

[36] D. Nicholson, *Introduction to Plasma Theory*, Wiley, New York, 1983.

[37] K. Nishikawa and M. Wakatani, *Plasma Physics*, Springer, Berlin, Heidelberg, 2000.

[38] H. Nussbaumer, *Fast Fourier Transform and Convolution Algorithms*, Springer, Berlin, Heidelberg, New York, 1981.

[39] W. H. Press, B. P. Flannery, S. A. Teukolsky, and W. T. Vetterling, *Numerical Recipes*, Cambridge University Press, Cambridge, 1987.

[40] J. Prussing and B. Conway, *Orbital Mechanics*, Oxford University Press, Oxford, 1993.

[41] J. Qiang, R. Ryne, and S. Habib, *Self-consistent Langevin simulation of Coulomb collisions in charged-particle beams*, Proceedings of the 2000 ACM/IEEE conference on Supercomputing (CD-ROM), Dallas, November 4-10, 2000.

[42] H. Risken, *The Fokker-Planck Equation*, Springer-Verlag, Berlin, 1989.

[43] M. Rosenbluth, W. MacDonald, and D. Judd, *Fokker-Planck equation for an inverse-square force*, Phys. Rev., 107 (1957), pp. 1–6.

[44] A. Sommerfeld, *Thermodynamik und Statistik, Band V*, Verlag Harri Deutsch, Thun, Frankfurt/M., 1977.

[45] M. Spiegel, *Vektoranalysis*, McGraw-Hill, Schaum's Outline, Hamburg, New York, 1984.

[46] R. Tolman, *The Principles of Statistical Mechanics*, Dover Publications, New York, 1979.

[47] A. Vikhansky and M. Kraft, *Conservative method for the reduction of the number of particles in the Monte Carlo simulation method for kinetic equations*, J. Comput. Phys., 203 (2005), pp. 371–378.

Appendix A. Boltzmann Collision Integral and Fokker-Planck Approximation

The Boltzmann collision interal (cf. [29, 13]) is given by

$$\left(\frac{\delta f_\alpha}{\delta t}\right)_{\rm col} = \sum_\beta n_\beta(\mathbf{x},t) \int d^3w\, d\Omega\; g\, Q_{\alpha\beta} \left[\Phi_{\alpha\beta}(\mathbf{c}',\mathbf{w}') - \Phi_{\alpha\beta}(\mathbf{c},\mathbf{w})\right] , \tag{116}$$

where $\Phi_{\alpha\beta}(\mathbf{c},\mathbf{w}) = f_\alpha(\mathbf{c})\, f_\beta(\mathbf{w})$ is the product of the test and field particle distribution functions. Here, the index β runs over all "scattering" populations (field particles), n_β is the local number density of the field particle specie "β", $g = |\mathbf{g}| = |\mathbf{c}-\mathbf{w}|$ is the absolute value of the relative velocity, $Q_{\alpha,\beta} = Q_{\alpha,\beta}(g,\chi,\varphi)$ is the differential scattering cross section (in the CM system) between the particles of the species "α" and "β" and the element of solid angle $d\Omega$ is given by $d\Omega = \sin\chi\, d\chi\, d\varphi$ (χ: scattering angle, φ: azimuthal angle). Moreover, the prime refers to the value of a quantity after a collision and unprimed denotes the values before the collision. In order to obtain from the collision integral (116) the Fokker-Planck approximation, the following laws and approximations are applied. First, to describe charged particles interaction we use the Rutherford differential scattering cross section (see Appendix B). During the elastic collision $\mathbf{g}$ is rotated to $\mathbf{g}' = \mathbf{c}' - \mathbf{w}'$ with $|\mathbf{g}'| = |\mathbf{g}|$ and, furthermore, $\mathbf{c}' = \mathbf{c} + \Delta\mathbf{c}$ and $\mathbf{w}' = \mathbf{w} + \Delta\mathbf{w}$ is assumed for small angle (large impact parameter) scattering, where $\Delta\mathbf{c}$ and $\Delta\mathbf{w}$ are, respectively, given by $\Delta\mathbf{c} = m_{\alpha\beta}/m_\alpha\, \Delta\mathbf{g}$ and $\Delta\mathbf{w} = -m_{\alpha\beta}/m_\beta\, \Delta\mathbf{g}$. Then, a Taylor series expansion of $\Phi_{\alpha\beta}(\mathbf{c}',\mathbf{w}')$ is performed up to second order. Taking into account conservation of momentum and performing some rearrangements, we can write $\Delta\mathbf{g} = \mathbf{g}' - \mathbf{g}$ according to

$$\Delta\mathbf{g} = g\, \vec{\omega}(\chi,\varphi) , \tag{117}$$

where the angle-dependent part is given by

$$\vec{\omega}(\chi,\varphi) = \begin{pmatrix} -2\sin^2(\chi/2) \\ \sin\chi\, \cos\varphi \\ \sin\chi\, \sin\varphi \end{pmatrix} . \tag{118}$$

Besides, the vector quantity (117) the tensor quantity

$$\Delta\mathbf{g}\, \Delta\mathbf{g}^T = g^2\, \vec{\omega}\, \vec{\omega}^T \tag{119}$$

appears in the resulting expression of the approximated Boltzmann collision integral. For small angle cut-off $\chi_{\rm min}$ (see Appendix B), the integration over the azimuthal and scattering angles yields

$$\begin{aligned} <\Delta\mathbf{g}> &= \int_0^{2\pi} d\varphi \int_{\chi_{\rm min}}^{\pi} d\chi\, \sin\xi\, Q_{\alpha\beta}(\chi,\varphi)\, \Delta\mathbf{g} \\ &= \frac{4\pi C^2}{m_{\alpha\beta}^2 g^2} \ln\left[\sin\left(\frac{\chi}{2}\right)\right] \mathbf{e}_x , \quad \mathbf{e}_x = \frac{\mathbf{g}}{g} \end{aligned} \tag{120}$$

for the vector and

$$< \Delta\mathbf{g}\,\Delta\mathbf{g}^T > \;=\; \int_0^{2\pi} d\varphi \int_{\chi_{\min}}^{\pi} d\chi\, \sin\chi\, Q_{\alpha\beta}(\chi,\varphi)\, \Delta\mathbf{g}\,\Delta\mathbf{g}^T$$

$$= \; -\frac{4\pi C^2}{m_{\alpha\beta}^2 g^2} \ln\left[\sin\left(\frac{\chi}{2}\right)\right] \frac{1}{g}\left(\mathbb{I} - \mathbf{e}_x\,\mathbf{e}_x^T\right) \qquad (121)$$

for the tensor quantity, where expressions like $8\pi\left[1+\cos\chi_{\min}\right]$ and $8\pi\cos^2\left(\chi_{\min}/2\right)$ are neglected, because they are very small compared to $\ln\left[\sin\left(\frac{\chi}{2}\right)\right]$ for small $\chi = \chi_{\min}$. After performing some straightforward but lengthy algebra, we finally obtaion the FP equation (1) given in Section 2, which represents the lowest order approximation to the Boltzmann integral (116) and takes into account small-angle scattering of point charges on the Coulomb potential.

Appendix B. Differential Rutherford Scattering Cross Section

The classical Rutherford differential scattering cross section of two charged particles of types "α" and "β" is given by (see, for instance [28])

$$Q_{\alpha\beta}(g,\chi,\varphi) = \frac{1}{4}\left(\frac{C}{m_{\alpha\beta}}\right)^2 \frac{1}{g^4\,\sin^4\left(\frac{\chi}{2}\right)} \tag{122}$$

where $m_{\alpha\beta}$ denotes the reduced mass and the constant C is given by $C = -\frac{q_\alpha\, q_\beta}{4\pi\,\epsilon_0}$. This result is obtained for a Coulomb potential ($V = C/r$) for which it is well-known that the total cross section for isotropic scattering

$$\sigma_T(g) = 2\pi \int^{\pi} Q_{\alpha\beta}(g,\chi)\,\sin\chi d\chi \tag{123}$$

diverges at the lower boundary ($\xi = 0$) as a consequence of this potential. Under the assumption that the Coulomb fields of all particles are screened by the collective behavior of these charges, the effective range of the Coulomb force may be estimated by the Debye length λ_D:

$$\frac{1}{\lambda_D^2} = \sum_\alpha \frac{n_\alpha\, q_\alpha^2}{\epsilon_0\, k\, T_\alpha}\,. \tag{124}$$

Clearly, this length represents a natural estimation of the maximal impact parameter $b_{\max} = \lambda_D$, to which the minimal cut-off scattering angle $\chi_{\min}$ is related according to

$$\sin\left(\frac{\chi}{2}\right) = \frac{b_0}{b}\left[1+\left(\frac{b_0}{b}\right)^2\right]^{-1/2} = \frac{1}{\sqrt{1+\left(\frac{b}{b_0}\right)^2}} \tag{125}$$

for $b = \lambda_D$, where $b_0 = \frac{|C|}{m_{\alpha\beta}\,g^2}$ is the impact parameter for $\chi = \pi/2$ scattering. In the case, where $b_0/\lambda_D \ll 1$, the minimal scattering angle is simply given by

$$\sin\left(\frac{\chi_{\min}}{2}\right) \approx \frac{b_0}{\lambda_D} = \frac{1}{\Lambda}\,, \tag{126}$$

where Λ is defined by $\Lambda = \lambda_D/b_0$ and can be interpreted as the measure of the number of particles in a sphere of radius λ_D and is sometimes called "*plasma parameter*" in the literature. For practical estimations and calculations it is sensible to approximate the mean kinetic energy roughly by the thermal energy – $\frac{1}{2}m_{\alpha\beta}\,g^2 \approx \frac{3}{2}\,k_{\rm B}\,T_\alpha$ – and replace b_0 by

$$\overline{b}_0 = \frac{|q_\alpha\, q_\beta|}{12\pi\epsilon_0\, k_{\rm B}\, T_\alpha}\,. \tag{127}$$

Clearly, expression (126) relates the small scattering angle cut-off to maximal impact parameter $b_{\max} = \lambda_D$, which reflects the collective screening in a plasma. Obviously, it is not amazing that the cut-off scattering angle $\chi_{\min}$ is responsible for the main contribution to the totat Coulomb cross section according to (123):

$$\sigma_T(g) = \pi\,\lambda_D^2\,. \tag{128}$$

Especially, if the parameter Λ is very large, large-angle collisions among plasma particles can be neglected and the collisional dynamics is dominated by small-angle collisions, which is well-modeled by the Fokker-Planck approach.

Appendix C. Short-time Solution of the FP equation

To obtain the short-time solution $S(\mathbf{c},t)$ of the FP equation (2) in Section 2 for given initial data

$$S_0(\mathbf{c},t) = \delta\Big(\mathbf{c}-\mathbf{c}_0\Big)\,, \tag{129}$$

it is sufficient to study the solution of the equation

$$\frac{\partial S}{\partial t} = -F_p\,\frac{\partial\, S}{dc_p} + D_{pq}\,\frac{\partial^2\, S}{\partial c_p \partial c_q}\,. \tag{130}$$

This is correct, because for small τ the solution of the FP equation will be sharply peaked and, hence, the derivatives of the friction $F_p = F_p(\mathbf{c},t)$ and the diffusion $D_{pq} = D_{pq}(\mathbf{c},t)$ coefficients can be neglected compared to those of S. Consequently, we will assume that F_p and D_{pq} are approximately constant within the time interval $[t,\, t+\tau]$. To find the solution of problem (130), we apply Fourier transformation techniques and exploit some properties of this transformation to obain the result

$$\hat{S}(\mathbf{k},\tau) = \frac{\mathrm{e}^{-i\mathbf{k}\cdot\mathbf{c}_0}}{(2\pi)^{3/2}}\,\exp\!\Big\{-\Big(i\mathbf{F}\cdot\mathbf{k}+\frac{1}{2}\mathbf{k}^T\,\mathbb{D}\,\mathbf{k}\Big)\,\tau\Big\}\,, \tag{131}$$

where τ denotes the small time increment. To get the inverse Fourier transformation of the latter equation we define the following auxiliary vector and matrix

$$\mathbf{V} \;=\; \mathbf{c}-\mathbf{c}_0-\tau\,\mathbf{F} \tag{132}$$

$$\tilde{\mathbb{D}} \;=\; \big[\tau\,\mathbb{I}\big]\,\mathbb{D}\,, \tag{133}$$

where $\mathbb{I}$ denotes the identity. Since the diffusion matrix $\mathbb{D}$ (and consequently $\tilde{\mathbb{D}}$) is a symmetric matrix, it is convenient to apply the substitution

$$\mathbf{z} = \mathbf{k} - i\,\tilde{\mathbb{D}}^{-1}\,\mathbf{V} \tag{134}$$

to find the relation

$$\mathbf{k}^T\,\tilde{\mathbb{D}}\mathbf{k} - 2i\,\mathbf{V}\cdot\mathbf{k} = \mathbf{z}^T\,\tilde{\mathbb{D}}\mathbf{z} + \mathbf{V}^T\,\tilde{\mathbb{D}}^{-1}\mathbf{V}\,. \tag{135}$$

To solve the remaining integral $\int\limits_{-\infty}^{\infty} d^3z\,\exp\!\Big\{-\frac{1}{2}\mathbf{z}^T\,\tilde{\mathbb{D}}\mathbf{z}\Big\}$, we once again apply the fact that $\tilde{\mathbb{D}}$ is symmetric, which guarantees that there exists an orthogonal matrix $\mathbb{O}$ with the property $\tilde{\mathbb{S}} = \mathbb{O}^T\,\tilde{\mathbb{D}}\,\mathbb{O} = \mathsf{diag}[\tilde{s}_1^2,\,\tilde{s}_2^2,\,\tilde{s}_3^2]$. Finally, a straightforward computation leads to the result

$$\begin{aligned} S(\mathbf{c},\tau) \;&=\; \frac{\sqrt{|\tilde{\mathbb{D}}^{-1}|}}{(2\pi)^{3/2}}\,\exp\!\Big\{-\frac{1}{2}\mathbf{V}^T\,\tilde{\mathbb{D}}^{-1}\mathbf{V}\Big\} \\ &=\; \frac{\sqrt{|\mathbb{D}^{-1}|}}{(2\pi\,\tau)^{3/2}}\,\exp\!\Big\{-\frac{1}{2\,\tau}\big(\delta\mathbf{c}-\tau\,\mathbf{F}\big)^T\,\mathbb{D}^{-1}\,\big(\delta\mathbf{c}-\tau\,\mathbf{F}\big)\Big\} \end{aligned} \tag{136}$$

which represents the back transformation of expression (131) and the solution of (130), where $\delta\mathbf{c} = \mathbf{c}-\mathbf{c}_0$. Clearly, this result represents a (two parameter) Gaussian distribution for $\delta\mathbf{c}$ with mean value $\tau\,\mathbf{F}$ and variance $\tau\,\mathbb{D}$. Note, that the matrix of the standard deviation $\mathbb{B}$ can be expressed according to

$$\sqrt{\tau}\,\mathbb{B} = \sqrt{\tau}\,\mathbb{O}\mathbb{S}^{1/2}\mathbb{O}^T\,,$$

where $\mathbb{O}$ is a orthogonal matrix and $\mathbb{S} = \mathbb{O}^T \mathbb{D} \mathbb{O} = \mathsf{diag}[s_1^2,\, s_2^2,\, s_3^2]$. Under the assumption that $\mathbb{D} = \mathsf{diag}[D_1,\, D_2,\, D_3]$ holds, we can immediately recast equation (136) into the form

$$S(\mathbf{c}, \tau) = \prod_{\alpha=1}^{3} \frac{1}{\sqrt{2\pi\,\tau}\,\sigma_\alpha} \exp\left\{ -\frac{(c_\alpha - \mu_\alpha)^2}{2\sigma_\alpha^2} \right\}, \tag{137}$$

where the abbreviations

$$\mu_\alpha = v_{0,\alpha} + \tau\, F_\alpha \quad \text{and} \quad \sigma_\alpha^2 = \tau\, D_\alpha \tag{138}$$

are used, which are, respectively, the mean value and the variance of the α^{th} Gaussian normal distribution.

Appendix D. Three Dimensional Solution of the Lenard-Bernstein Model

In the following we briefly sketch the analytical solution of the Lenard-Bernstein model (see, [37] for the one-dimensional and [12, 42] for the three-dimensional case), which is also known in the literature as the Ornstein-Uhlenbeck process. The model is established by the assumption that the friction force and the (symmetric) diffusion tensor are given by

$$\mathbf{F}(\mathbf{x},\mathbf{c},t) = -\mathbb{A}\mathbf{c} \quad \text{and} \quad \mathbb{D}(\mathbf{x},\mathbf{c},t) = \mathbb{D}(\mathbf{x},t)\ , \tag{139}$$

where the matrix $\mathbb{A} \in \mathbb{R}^{3\times 3}$, in general, may be depend on $\mathbf{x}$ and t. Then, the FP equation for the transition probability $P(\mathbf{c},t) = P(\mathbf{c},t|(\mathbf{c}_0,t_0)$ can be written as

$$\partial_t P(\mathbf{c},t) - A_{pq}\, c_q\, \frac{\partial P(\mathbf{c},t)}{\partial c_p} = Tr(\mathbb{A})P(\mathbf{c},t) + \frac{1}{2}D_{pq}\,\frac{\partial^2 P(\mathbf{c},t)}{\partial c_p \partial c_q}\ , \tag{140}$$

where $Tr(\mathbb{A})$ denotes the trace of the matrix $\mathbb{A}$. This equation is complemented by the initial condition $P_0(\mathbf{c}) = P(\mathbf{c},t_0|\mathbf{c}_0,t_0) = \delta(\mathbf{c}-\mathbf{c}_0)$. In order to replace the left-hand side of the latter equation by the substantial derivative, we introduce the variable transformation

$$\mathbf{u} = \mathrm{e}^{\mathbb{A}\,(t-t_0)}\mathbf{c} \quad \Leftrightarrow \quad \mathbf{c} = \mathrm{e}^{-\mathbb{A}\,(t-t_0)}\mathbf{u} \tag{141}$$

and get after some algebra the equation for $P(\mathbf{u},t) = P(\mathbf{u},t|\mathbf{u}_0,t_0)$

$$\frac{dP(\mathbf{u},t)}{dt} = Tr(\mathbb{A})\,P(\mathbf{u},t) + \frac{1}{2}\nabla_u^T\,\mathrm{e}^{\mathbb{A}\,(t-t_0)}\,\mathbb{D}\,\mathrm{e}^{\mathbb{A}^T\,(t-t_0)}\,\nabla_u\,P(\mathbf{u},t) \tag{142}$$

with the initial data $P_0(\mathbf{u}) = P(\mathbf{u},t_0|\mathbf{u}_0,t_0) = \delta(\mathbf{u}-\mathbf{u}_0)$. Applying a Fourier transformation according to $\hat{P}(\mathbf{k},t) = \frac{1}{\left(2\pi\right)^{3/2}}\int\limits_{-\infty}^{\infty} d^3u\,\mathrm{e}^{-i\mathbf{k}\cdot\mathbf{u}}P(\mathbf{u},t)$, yields an ordinary differential equation in time whose solution reads as

$$\hat{P}(\mathbf{k},t) = \frac{1}{\left(2\pi\right)^{3/2}}\exp\left\{Tr(\mathbb{A})\,(t-t_0) - i\mathbf{u}_0^T\,\mathbf{k} - \frac{1}{2}\mathbf{k}^T\,\mathbb{M}\,\mathbf{k}\right\}\ , \tag{143}$$

where the initial condition $\hat{P}_0(\mathbf{k}) = \frac{1}{(2\pi)^{3/2}}\mathrm{e}^{-i\mathbf{k}\cdot\mathbf{u}_0}$ already has been inserted and $\mathbb{M}$ is given by

$$\mathbb{M} = \int\limits_{t_0}^{t} \mathrm{e}^{\mathbb{A}\,(s-t_0)}\,\mathbb{D}\,\mathrm{e}^{\mathbb{A}^T\,(s-t_0)}ds\ . \tag{144}$$

To perform the integration with respect to time, we consider

$$\mathrm{e}^{\mathbb{A}\,(s-t_0)}\,\mathbb{D}\,\mathrm{e}^{\mathbb{A}^T\,(s-t_0)} = \frac{d}{ds}\left[\mathrm{e}^{\mathbb{A}\,(s-t_0)}\,\mathbb{G}\,\mathrm{e}^{\mathbb{A}^T\,(s-t_0)}\right] \tag{145}$$

and conclude that $\mathbb{G}$ has to be a symmetric matrix (since $\mathbb{D}$ is symmetric) defined by

$$\mathbb{D} = \mathbb{A}\mathbb{G} + \mathbb{G}\mathbb{A}^T\ . \tag{146}$$

Then expression (144) reads as

$$\mathbb{M} = \mathrm{e}^{\mathbb{A}\,(t-t_0)}\,\mathbb{G}\,\mathrm{e}^{\mathbb{A}^T\,(t-t_0)} - \mathbb{G} \tag{147}$$

which reveals that $\mathbb{M}$ is also a (real) symmetric matrix. Performing the inverse Fourier transformation of the expression (143) we obtain the intermediate result

$$P(\mathbf{u},t) = \frac{\mathrm{e}^{Tr(\mathbb{A})\,(t-t_0)}}{(2\pi)^3} \int\limits_{-\infty}^{\infty} d^3k\, \exp\Big\{ -\frac{1}{2}\mathbf{k}^T\,\mathbb{M}\,\mathbf{k} + i\,\mathbf{V}^T\mathbf{k} \Big\}\,, \tag{148}$$

where the abbreviation $\mathbf{V} = \mathbf{u} - \mathbf{u}_0$ is introduced. With the auxiliary vector

$$\mathbf{x} = \mathbf{k} - i\,\mathbb{M}^{-1}\,\mathbf{V} \tag{149}$$

the exponent of the integrand can be reformulated in such a way that only the integral $\int\limits_{-\infty}^{\infty} d^3x\, \exp\Big\{ -\frac{1}{2}\mathbf{x}^T\,\mathbb{M}\,\mathbf{x} \Big\}$ has to be evaluated. Since $\mathbb{M}$ is symmetric, we can find the (orthogonal) eigenvector matrix $\mathbb{B}$ of $\mathbb{M}$ which has the property $\mathbb{B}^T\,\mathbb{M}\mathbb{B} = \mathrm{diag}[\lambda_1,\,\lambda_2,\,\lambda_3]$. With the new vector $\mathbf{y} = \mathbb{B}^{-1}\,\mathbf{x}$ and the fact that $d^3x = |\mathbb{B}|\,d^3y$ we can perform the integration and finally obtain for the distribution function

$$P(\mathbf{u},t) = \mathrm{e}^{Tr(\mathbb{A})\,(t-t_0)}\frac{\sqrt{|\mathbb{M}^{-1}|}}{(2\pi)^{3/2}}\exp\Big\{ -\frac{1}{2}\mathbf{V}^T\mathbb{M}^{-1}\,\mathbf{V} \Big\}\,, \tag{150}$$

where $\mathbb{M}^{-1}$ is the inverse of (147). Switching back to the original variables $\mathbf{c}$ according to (141), we immediately get

$$P(\mathbf{c},t) = \frac{\sqrt{|\mathbb{H}|}}{(2\pi)^{3/2}}\exp\Big\{ -\frac{1}{2}\Big(\mathbf{c} - \mathrm{e}^{-\mathbb{A}\,(t-t_0)}\,\mathbf{c}_0\Big)^T\,\mathbb{H}\,\Big(\mathbf{c} - \mathrm{e}^{-\mathbb{A}\,(t-t_0)}\,\mathbf{c}_0\Big) \Big\}\,, \tag{151}$$

where $\mathbb{H} = \mathrm{e}^{\mathbb{A}^T\,(t-t_0)}\,\mathbb{M}^{-1}\,\mathrm{e}^{\mathbb{A}\,(t-t_0)}$ and the identity $|\mathrm{e}^{\mathbb{A}\tau}| = \mathrm{e}^{Tr(\mathbb{A})\tau}$ is taken into account. Furthermore, we note that the transition probability is normalized:

$$\int\limits_{-\infty}^{\infty} d^3c\, P(\mathbf{c},t) = 1\,. \tag{152}$$

Using the identities

$$\nabla_\xi \mathrm{e}^{-\frac{1}{2}\xi^T\,\mathbb{H}\,\xi} = -\mathbb{H}\xi\,\mathrm{e}^{-\frac{1}{2}\xi^T\,\mathbb{H}\,\xi}$$

and

$$\nabla_\xi\,\nabla_\xi^T \mathrm{e}^{-\frac{1}{2}\xi^T\,\mathbb{H}\,\xi} = \Big(\mathbb{H}\xi\,\xi^T\,\mathbb{H} - \mathbb{H}\xi\Big)\,\mathrm{e}^{-\frac{1}{2}\xi^T\,\mathbb{H}\,\xi}$$

with $\xi = \mathbf{c} - \hat{\mathbf{c}}_0$, we conclude and that the first moment and the variance are given by

$$< \mathbf{c} >= \int\limits_{-\infty}^{\infty} d^3c\,\mathbf{c}\,P(\mathbf{c},t) = \hat{\mathbf{c}}_0 = \mathrm{e}^{-\mathbb{A}(t-t_0)}\,\mathbf{c}_0 \tag{153}$$

and

$$< (\mathbf{c} - \hat{\mathbf{c}}_0)(\mathbf{c} - \hat{\mathbf{c}}_0)^T >=< (\mathbf{c}\,\mathbf{c}^T > -\hat{\mathbf{c}}_0\,\hat{\mathbf{c}}_0^T = \mathbb{H}^{-1} \tag{154}$$

respectively, where we assumed that the integrals of $\mathrm{e}^{-\frac{1}{2}\xi^T\,\mathbb{H}\,\xi}$ and $\nabla^T\,\mathrm{e}^{-\frac{1}{2}\xi^T\,\mathbb{H}\,\xi}$ over a surface vanish at infinity.

Appendix E. Some Properties of the Rosenbluth Potentials

The main interesting properties of the Rosenbluth potentials can be traced back to the following identities for $\mathbf{g} = \mathbf{v} - \mathbf{w}$ and $g = |\mathbf{v} - \mathbf{w}|$:

$$\nabla_v g = \frac{\mathbf{g}}{g} \tag{155}$$

$$\nabla_v \left(\frac{1}{g}\right) = -\frac{\mathbf{g}}{g^3} \tag{156}$$

$$\nabla_v \cdot \mathbf{g} = 3 \tag{157}$$

$$\nabla_v \cdot \Big[\nabla_v g\Big] = \nabla_v^2 \, g = \frac{2}{g} \tag{158}$$

$$\nabla_v \cdot \left[\nabla_v \Big(\frac{1}{g}\Big)\right] = \nabla_v^2 \left(\frac{1}{g}\right) = \begin{cases} 0\,, & \mathbf{v} \neq \mathbf{w} \\ -4\pi\delta\Big(\mathbf{v} - \mathbf{w}\Big)\,, & \mathbf{v} = \mathbf{w} \end{cases}, \tag{159}$$

where $\delta\Big(\mathbf{v} - \mathbf{w}\Big)$ is the Dirac distribution. Applying the latter relations to the potentials $\mathcal{H}^{(\beta)}$ and $\mathcal{G}^{(\beta)}$, we immediately obtain

$$\nabla_v^2 \, \mathcal{H}^{(\beta)}(\mathbf{x}, \mathbf{v}, t) = -4\pi \, \frac{m_\alpha}{\mu_{\alpha\beta}} \, f_\beta(\mathbf{x}, \mathbf{v}, t) \tag{160}$$

and

$$\nabla_v^2 \, \mathcal{G}^{(\beta)}(\mathbf{x}, \mathbf{v}, t) = 2\frac{\mu_{\alpha\beta}}{m_\alpha} \, \mathcal{H}^{(\beta)}(\mathbf{x}, \mathbf{v}, t)\,, \tag{161}$$

which means, that the potentials $\mathcal{H}^{(\beta)}$ and $\mathcal{G}^{(\beta)}$ are determined by the solution of Poisson equations with sources proportional to f_β and $\mathcal{H}^{(\beta)}$, respectively.

Appendix F. Fourier Transformation of the Coulomb Potential

In order to obtain the Fourier transformation of the Coulomb potential $1/g$ $\Big(g = |\mathbf{v} - \mathbf{w}|\Big)$, it is convenient to start from the Yukawa (or Debye) potential

$$\varphi_\eta(\mathbf{g}) = \frac{\mathrm{e}^{-\eta\, g}}{g}\,, \tag{162}$$

where η is a positive real number. Clearly, in the limit $\eta \to 0$ one recovers the usual Coulomb potential. The Fourier transformation of the latter equation

$$\hat{\varphi}_\eta(\mathbf{k}) = \mathcal{F}\left\{\frac{\mathrm{e}^{-\eta\, g}}{g}\right\} = \frac{1}{(2\pi)^{3/2}} \int\limits_{-\infty}^{\infty} d^3g\, \mathrm{e}^{-i\mathbf{k}\cdot\mathbf{g}}\, \frac{\mathrm{e}^{-\eta\, g}}{g} \tag{163}$$

can be determined analytically. For that, one introduces spherical coordinates in $\mathbf{g}$-space, perform the integration over the azimuthal and polar angle and get

$$\hat{\varphi}_\eta(\mathbf{k}) \frac{1}{i\sqrt{2\pi}k} \int\limits_0^{\infty} dg\, \mathrm{e}^{-\eta\, g} \left(\mathrm{e}^{ikg} - \mathrm{e}^{-ikg}\right). \tag{164}$$

The final integration yields the Fourier transformation of the Yukawa potential given by

$$\hat{\varphi}_\eta(\mathbf{k}) = \frac{2}{\sqrt{2\pi}}\, \frac{1}{k^2 + \eta^2}\,, \tag{165}$$

from which one obtains immediately the Fourier transformation of the Coulomb potential in the limit $\eta \to 0$:

$$\hat{\varphi}(\mathbf{k}) = \frac{2}{\sqrt{2\pi}\, k^2}\,. \tag{166}$$

Appendix G. Approximate Multiple Stratonovich Integrals

In the following we adopt the notation of Kloeden et al. [24] and summarize the approximation of multiple Stratonovich integrals up to multiplicity two. One gets

$$\mathrm{J}^P_{(0)} = \Delta t \;, \quad \mathrm{J}^P_{(j)} = \sqrt{\Delta t}\,\xi_j \;, \quad \mathrm{J}^P_{(0,0)} = \frac{1}{2}\,\Delta t^2 \;, \tag{167}$$

$$\mathrm{J}^P_{(j,0)} = \frac{\Delta t}{2}\Big(\sqrt{\Delta t}\,\xi_j + a_{j,0}\Big) \;, \quad \mathrm{J}^P_{(0,j)} = \frac{\Delta t}{2}\Big(\sqrt{\Delta t}\,\xi_j - a_{j,0}\Big) \;, \tag{168}$$

where

$$a_{j,0} = -\frac{1}{\pi}\sqrt{2\Delta t}\sum_{r=1}^{P}\frac{1}{r}\,\zeta_{j,r} - 2\sqrt{\Delta t\;\rho_P}\;\mu_j^{(P)}$$

$$\mathrm{J}^P_{(j_1,j_2)} = \frac{\Delta t}{2}\,\xi_{j_1}\,\xi_{j_2} - \frac{1}{2}\sqrt{\Delta t}\,\Big(a_{j_2,0}\,\xi_{j_1} - a_{j_1,0}\,\xi_{j_2}\Big) + \Delta t\,A^P_{j_1,j_2} \tag{169}$$

with

$$A^P_{j_1,j_2} = \frac{1}{2\pi}\sum_{r=1}^{P}\frac{1}{r}\,\Big(\zeta_{j_1,r}\,\eta_{j_2,r} - \eta_{j_1,r}\,\zeta_{j_2,r}\Big)\;.$$